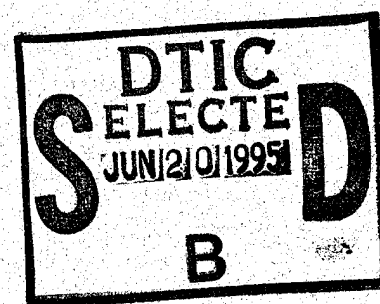


## Quarterly Technical Report

## Solid State Research



1994:4

---

**Lincoln Laboratory**  
MASSACHUSETTS INSTITUTE OF TECHNOLOGY  
*LEXINGTON, MASSACHUSETTS*



---

Prepared for the Department of the Air Force under Contract F19628-95-C-0002.

Approved for public release; distribution is unlimited.

19950616 052

DTIC QUALITY INSPECTED 8

**This report is based on studies performed at Lincoln Laboratory, a center for research operated by Massachusetts Institute of Technology. The work was sponsored by the Department of the Air Force under Contract F19628-95-C-0002.**

**This report may be reproduced to satisfy needs of U.S. Government agencies.**

**The ESC Public Affairs Office has reviewed this report, and it is releasable to the National Technical Information Service, where it will be available to the general public, including foreign nationals.**

**This technical report has been reviewed and is approved for publication.**

**FOR THE COMMANDER**

  
Gary Tutungian  
Administrative Contracting Officer  
Contracted Support Management

Non-Lincoln Recipients

PLEASE DO NOT RETURN

Permission is given to destroy this document  
when it is no longer needed.

MASSACHUSETTS INSTITUTE OF TECHNOLOGY  
LINCOLN LABORATORY

**SOLID STATE RESEARCH**

**QUARTERLY TECHNICAL REPORT**

1 AUGUST — 31 OCTOBER 1994

ISSUED 28 APRIL 1995

Approved for public release; distribution is unlimited.

LEXINGTON

MASSACHUSETTS

## ABSTRACT

This report covers in detail the research work of the Solid State Division at Lincoln Laboratory for the period 1 August through 31 October 1994. The topics covered are Electrooptical Devices, Quantum Electronics, Materials Research, Submicrometer Technology, High Speed Electronics, Microelectronics, and Analog Device Technology. Funding is provided primarily by the Air Force, with additional support provided by the Army, ARPA, Navy, BMDO, NASA, and NIST.

<b>Accession For</b>	
NTIS GEM&I	<input checked="" type="checkbox"/>
DTIC TAB	<input type="checkbox"/>
Unannounced	<input checked="" type="checkbox"/>
Justification	
By	
Distribution/	
Availability Codes	
Dist	Avail and/or Special
A-1	

## TABLE OF CONTENTS

Abstract	iii
List of Illustrations	vii
List of Tables	ix
Introduction	xi
Reports on Solid State Research	xiii
Organization	xxiii
 1. ELECTROOPTICAL DEVICES	 1
1.1 Two-Sided Anamorphic Microlens for Compact High-Power Diode Laser System	1
 2. QUANTUM ELECTRONICS	 5
2.1 Coupled-Cavity Electrooptically <i>Q</i> -Switched Nd:YVO <sub>4</sub> Microchip Lasers	5
2.2 Thermal Evaporation of Low-Impedance Al-AlO <sub>x</sub> Pb Junctions	10
 3. MATERIALS RESEARCH	 15
3.1 High-Power, High-Temperature Operation of GaInAsSb-AlGaAsSb Ridge-Waveguide Lasers Emitting at 1.9 $\mu\text{m}$	15
 4. SUBMICROMETER TECHNOLOGY	 19
4.1 Integrated Circuit Interconnect Technique for High-Density Applications	19
4.2 Single-Layer Resists with Enhanced Etch Resistance for 193-nm Lithography	22
 5. HIGH SPEED ELECTRONICS	 27
5.1 Staggered-Barrier Heterostructure Insulated-Gate Field-Effect Transistor on InP	27
 6. MICROELECTRONICS	 31
6.1 Improved Soft X-Ray Quantum Efficiency for Back-Illuminated Imager	31
 7. ANALOG DEVICE TECHNOLOGY	 33
7.1 Analysis of the Quantum Flux Parametron for Sensing Small Currents at High Bandwidths	33

## LIST OF ILLUSTRATIONS

Figure No.		Page
1-1	Schematic of present two-sided anamorphic microlens, which couples output from high-power tapered laser directly to single-mode fiber.	1
1-2	Optical micrograph of fabricated two-sided microlens wafer viewed from cylindrical lens side. The spherical lenses on the back side can also be seen through the transparent GaP substrate.	2
1-3	Stylus surface profiles of spherical and cylindrical sides of microlens.	3
1-4	High-power tapered-laser output focused by two-sided anamorphic microlens. The overexposed photograph on the right shows some diffraction sidelobes.	3
2-1	Coupled-cavity electrooptically <i>Q</i> -switched microchip laser (HR, highly reflecting; AR, antireflecting).	6
2-2	Effective cavity round-trip time vs gain for optimized coupled-cavity <i>Q</i> -switched laser with $m_l = 1$ and $m_l = 2$ .	8
2-3	Oscilloscope trace of 115-ps pulse from coupled-cavity <i>Q</i> -switched Nd:YVO <sub>4</sub> microchip laser pumped with 0.5 W of incident CW diode power. The impulse response of the detector is 60 ps in duration; the afterpulse in the trace is the result of electrical ringing in the detector.	9
2-4	Pulse width as function of pulse repetition rate for coupled-cavity <i>Q</i> -switched Nd:YVO <sub>4</sub> microchip laser pumped with 1.2 W of incident CW diode power.	9
2-5	Oxygen exposure profiles for 5-, 6-, 8-, and 10-min. cycles used in junction fabrication process.	11
2-6	Junction impedance resulting from different exposure times, measured one day after fabrication. Only data from processes with similar parameters are plotted.	13
2-7	Impedance stability of junctions of differing lead contact thickness showing improved stability with thicker passivation and greater absolute increases resulting from junctions of higher starting impedance.	13
3-1	Output power vs current of 1000- $\mu$ m-long GaInAsSb/AlGaAsSb ridge-waveguide laser at 20°C. The front and back facets are coated to have reflectivity < 1% and > 95%, respectively.	16
3-2	Emission spectrum of GaInAsSb/AlGaAsSb ridge-waveguide laser at CW power of 40 mW.	17

## LIST OF ILLUSTRATIONS (Continued)

Figure No.		Page
3-3	Output power vs current for CW operation of 1000- $\mu$ m-long GaInAsSb/AlGaAsSb ridge-waveguide laser at several heatsink temperatures.	17
4-1	Scanning electron micrograph of platinum beam leads fabricated on integrated circuit chip. In this test pattern, the short U-shaped wires form a continuity structure when combined with the solder bumps and wiring on the multichip module (MCM) substrate. The long U-shaped wires provide contact to the bonding pads on the chip.	19
4-2	Solder bump fabrication processing steps: (a) MCM substrate, (b) titanium and copper deposited to form the under-bump metallization, (c) locations for solder bumps defined in photoresist, (d) electroplating of lead and tin, (e) stripping of photoresist, copper, and titanium (the solder bumps mask the removal of the copper and titanium on the pads), and (f) alloying the lead/tin aggregate to form the solder bumps.	20
4-3	Scanning electron micrograph of solder bumps fabricated on MCM substrate.	21
4-4	Etch rate of methacrylate copolymers as function of alicyclic content.	23
5-1	Room-temperature common-source current-voltage characteristics of (a) conventional $\text{In}_{0.53}\text{Ga}_{0.47}\text{As}/\text{In}_{0.52}\text{Al}_{0.48}\text{As}$ heterostructure insulated-gate field-effect transistor (HIGFET) on InP substrate and (b) staggered-barrier (SB) HIGFET containing two 2.0-nm-thick AlAs barriers just above $\text{In}_{0.53}\text{Ga}_{0.47}\text{As}$ channel.	28
5-2	Room-temperature gate current vs gate voltage measured with drain and source contacts grounded for conventional $\text{In}_{0.53}\text{Ga}_{0.47}\text{As}/\text{In}_{0.52}\text{Al}_{0.48}\text{As}$ HIGFET on InP substrate and SB-HIGFET containing two 2.0-nm-thick AlAs barriers just above $\text{In}_{0.53}\text{Ga}_{0.47}\text{As}$ channel.	29
6-1	Frequency of single events vs energy for back-illuminated imager exposed to C K $\alpha$ x-rays.	31
7-1	Schematic diagram of quantum flux parametron (QFP) used as current comparator. The dashed line surrounds the output inductor to emphasize that it is a shunt across the SQUID loop comprising the elements $J_1, L_1, L_2, J_2$ .	34
7-2	Potential energy plots of QFP for different input/exciter conditions. The abscissa is the magnetic flux ( $\Phi$ ) in the output inductor $L_{\text{out}}$ . In (a) neither the input nor the exciter current has been applied. Then a small negative input current is applied in (b). In (c) we have begun to ramp up the exciter, and in (d) the exciter is at its final value.	34

## LIST OF ILLUSTRATIONS (Continued)

Figure No.		Page
7-3	Schematic diagram of QFP showing terminology used to compute the static solutions. The exciter current couples $\alpha_1$ radians of phase into the inductor $L_1$ and $\alpha_2$ radians of phase into the inductor $L_2$ . The input couples $\beta$ radians of phase into the inductor $L_{out}$ .	35
7-4	Plots of QFP solutions for circuit parameters: $L_1 = L_2 = 0.9$ pH, $I_{c1} = I_{c2} = 225$ $\mu$ A, $L_{out} = 4.1857$ pH, $\beta = 0.1$ rad, $\alpha = \{-2\pi, 2\pi\}$ . In (a) we show all solutions and in (b) we show only stable equilibria.	37

## LIST OF TABLES

Table No.		Page
4-1	Characteristics of MMA/IBMA Copolymers	23



## INTRODUCTION

### 1. ELECTROOPTICAL DEVICES

A novel two-sided anamorphic microlens has been fabricated by mass transport and is capable of coupling the astigmatic output of high-power tapered diode lasers directly into a single-mode fiber. A high level of fiber-coupled power of 347 mW at 980 nm wavelength has been obtained, which demonstrates a new capability for miniaturizing high-power fiber-coupled diode laser systems.

### 2. QUANTUM ELECTRONICS

Nd:YVO<sub>4</sub> microchip lasers have been electrooptically *Q*-switched to produce 12- $\mu$ J pulses of 115-ps duration at repetition rates up to 1 kHz. At a repetition rate of 2.25 MHz, 0.16- $\mu$ J pulses were obtained with an 8.8-ns duration.

A method for the fabrication of low-impedance Al-AlO<sub>x</sub>-Pb junctions has been developed, and limited control over junction impedance has been demonstrated by varying the oxygen exposure time of a freshly evaporated aluminum contact. Chamber prebaking and evaporative gettering are found to play the dominant role in limiting the AlO<sub>x</sub> oxide growth, resulting in junctions with much lower impedance than otherwise possible, and absolute impedance stability is shown to depend on starting impedance and thickness of the lead contact, which acts as a barrier for the migration of atmospheric oxygen.

### 3. MATERIALS RESEARCH

Record-performance single-mode ridge-waveguide lasers emitting at 1.9  $\mu$ m have been fabricated from low-threshold laser material consisting of compressively strained multiple-quantum-well GaInAsSb active layers and AlGaAsSb barrier/confining layers grown on GaSb substrates. These devices operated CW at temperatures up to 130°C, and at room temperature had diffraction-limited single-ended output as high as 100 mW.

### 4. SUBMICROMETER TECHNOLOGY

A novel high-density interconnection technique has been developed for fabricating prototype multichip modules using commercially available integrated circuit chips. Electroplated solder bumps are combined with laser-defined platinum beam leads to form the connections.

The dry etch resistance of the methyl-methacrylate-based 193-nm photoresist has been improved by the introduction of polymers containing isobornyl methacrylate. The effect of polymer composition on etch rate, aqueous solubility, and glass transition temperature has been investigated.

## **5. HIGH SPEED ELECTRONICS**

A normally-off InP-based field-effect transistor (FET) has been demonstrated that incorporates two thin, closely spaced barriers of AlAs embedded in the  $\text{In}_{0.52}\text{Al}_{0.48}\text{As}$  insulating layer to suppress forward-bias current between the  $\text{In}_{0.53}\text{Ga}_{0.47}\text{As}$  channel and the metal gate. The transistor yields up to 50 times less forward-bias gate current than conventional InP-based FETs with uniform  $\text{In}_{0.52}\text{Al}_{0.48}\text{As}$  insulating layers, and also displays a 50% higher forward-bias gate turn-on voltage, a 300% greater maximum drain current, and a 70% larger peak transconductance under common-source conditions.

## **6. MICROELECTRONICS**

The techniques used to produce ultraviolet-sensitive back-illuminated charge-coupled devices and dislocation slip-free silicon have been combined to fabricate imagers with good sensitivity to a broad band of x-rays. Absolute quantum efficiencies of 70% and good linewidths have been obtained for C K $\alpha$  x-rays.

## **7. ANALOG DEVICE TECHNOLOGY**

An algorithm and computer program have been developed to analyze the steady-state response of a Josephson-junction superconductive circuit, the quantum flux parametron. This circuit will serve as a very sensitive ( $\sim 1 \mu\text{A}$ ), very wideband (2 GHz) comparator in two chip designs—the programmable filter for a spread-spectrum modem and a digital crossbar switch.

## REPORTS ON SOLID STATE RESEARCH

1 AUGUST THROUGH 31 OCTOBER 1994

### PUBLICATIONS

- |   |   |   |
|---|---|---|
| Microstructural Dependence of Sputtered $\text{YBa}_2\text{Cu}_3\text{O}_{7-x}$ Thin Films on Deposition Parameters   | D. Bhatt*<br>S. N. Basu*<br>A. C. Westerheim*<br>A. C. Anderson                               | <i>Physica C</i> <b>222</b> , 283 (1994)                          |
| Modeling of Resist Performance  | M. A. Hartney   | <i>Adv. Mater. Opt. Electron.</i> <b>4</b> , 165 (1994)           |
| High-Power Diode-Laser-Pumped Midwavelength Infrared $\text{HgCdTe/CdZnTe}$ Quantum-Well Lasers   | H. Q. Le<br>J. M. Arias*<br>M. Zandian*<br>R. Zucca*<br>Y.-Z. Liu*                            | <i>Appl. Phys. Lett.</i> <b>65</b> , 810 (1994)                   |
| Full-Wave Analysis of Superconducting Microstrip Lines on Anisotropic Substrates Using Equivalent Surface Impedance Approach  | L. H. Lee<br>W. G. Lyons<br>T. P. Orlando*<br>S. M. Ali*<br>R. S. Withers*                    | <i>IEEE Trans. Microwave Theory Tech.</i> <b>41</b> , 2359 (1993) |
| Modified Two-Fluid Model for Superconductor Surface Impedance Calculation   | D. S. Linden*<br>T. P. Orlando<br>W. G. Lyons   | <i>IEEE Trans. Appl. Superconduct.</i> <b>4</b> , 136 (1994)      |
| Carrier-Gain Dynamics in $\text{In}_x\text{Ga}_{1-x}\text{As}/\text{Al}_y\text{Ga}_{1-y}\text{As}$ Strained-Layer Single-Quantum-Well Diode Lasers: Comparison of Theory and Experiment | G. D. Sanders*<br>C.-K. Sun*<br>J. G. Fujimoto*<br>H. K. Choi<br>C. A. Wang<br>C. J. Stanton* | <i>Phys. Rev. B</i> <b>50</b> , 8539 (1994)                       |

---

\*Author not at Lincoln Laboratory.

Effect of Radiation Trapping on  
Fluorescence Lifetime and Emission  
Cross Section Measurements in  
Solid-State Laser Media

D. S. Sumida\*  
T. Y. Fan

*Opt. Lett.* **19**, 1343 (1994)

Microchannel Heat Sinks for Two-  
Dimensional Diode Laser Arrays

J. N. Walpole  
L. J. Missaggia

*In Surface Emitting  
Semiconductor Lasers and  
Arrays*, J. M. Hammer and  
G. A. Evans, eds. (Academic,  
Orlando, Fla.)

Horizontal Cavity Surface Emitting  
Lasers with Integrated Beam  
Deflectors

R. C. Williamson  
J. P. Donnelly  
Z. L. Liau  
W. D. Goodhue  
J. N. Walpole

*In Surface Emitting  
Semiconductor Lasers and  
Arrays*, J. M. Hammer and  
G. A. Evans, eds. (Academic,  
Orlando, Fla.)

Diode-Pumped Passively *Q*-Switched  
Picosecond Microchip Lasers

J. J. Zayhowski  
C. Dill III

*Opt. Lett.* **19**, 1427 (1994)

#### ACCEPTED FOR PUBLICATION

A New Face-Centered-Cubic Photonic  
Crystal for Microwave and Millimeter-  
Wave Applications

K. Agi\*  
E. R. Brown  
C. Dill III  
O. B. McMahon  
K. M. Molvar  
K. J. Malloy\*

*Microwave Opt. Technol. Lett.*

Design of Ultra-Wideband Photonic  
Crystals for Broadband Antenna  
Applications

K. Agi\*  
E. R. Brown  
O. B. McMahon  
K. J. Malloy  
C. Dill III

*Appl. Phys. Lett.*

---

\*Author not at Lincoln Laboratory.

N-type III-V Multiple Quantum Well  
Detectors Exhibiting Normal-  
Incidence Response

E. R. Brown  
S. J. Eglash  
K. A. McIntosh

*In III-V Semiconductor  
Quantum Wells and  
Superlattices for Long  
Wavelength Infrared  
Detectors* (Artech House,  
Dedham, Mass.)

Self-Aligned GaAs MISFET's with a  
Low-Temperature-Grown GaAs  
Gate Insulator

C. L. Chen  
L. J. Mahoney  
K. B. Nichols  
M. J. Manfra  
B. F. Gramstorff  
K. M. Molvar  
R. A. Murphy  
E. R. Brown

*IEEE Electron Device Lett.*

3.9- $\mu\text{m}$  InAsSb/AlAsSb Double-  
Heterostructure Diode Lasers with  
High Output Power and Improved  
Temperature Characteristics

H. K. Choi  
G. W. Turner  
Z. L. Liao

*Appl. Phys. Lett.*

Strained-Layer InGaAsP Diode Lasers  
with Tapered Gain Region for  
Operation at  $\lambda = 1.3 \mu\text{m}$

S. H. Groves  
J. P. Donnelly  
J. N. Walpole  
J. D. Woodhouse  
L. J. Missaggia  
R. J. Bailey  
A. Napoleone

*IEEE Photon. Technol. Lett.*

A Direct Observation of the Electric  
Field Gradient Near Field-Emission  
Cathodes

Y. Liang\*  
D. Bonnell\*  
W. D. Goodhue  
D. D. Rathman  
C. O. Bozler

*Appl. Phys. Lett.*

Heterodyne Nondegenerate Pump-  
Probe Measurement Technique for  
Guided Wave Devices

C.-K. Sun\*  
B. Golubovic\*  
J. G. Fujimoto\*  
H. K. Choi  
C. A. Wang

*Opt. Lett.*

---

\*Author not at Lincoln Laboratory.

Tm:YVO<sub>4</sub> Microchip Lasers

J. J. Zayhowski  
C. Dill III  
J. Ochoa  
J. Harrison\*

*Appl. Opt.*

# PRESENTATIONS<sup>†</sup>

High-Power Monolithic Tapered  
Semiconductor Oscillators

J. N. Walpole

Workshop on Applications  
to Semiconductor Lasers and  
Critical Self-Focusing of  
Ultra-Short Laser Pulses,  
Cork, Ireland,  
24 August 1994

Aqueous-Base Developable 193-nm  
Resists Employing Etch Resistant  
Monomeric Dissolution Inhibitors

R. R. Kunz  
R. D. Allen\*  
G. M. Wallraff\*

American Chemical Society  
National Symposium,  
Washington,  
District of Columbia,  
24-25 August 1994

GaInAsSb Mid-Infrared Diode Lasers

D. L. Spears

Conference on Lasers and  
Electro-Optics Europe '94,  
Amsterdam, Netherlands,  
28 August–2 September 1994

The 193-nm Full-Field Step-and-Scan  
Prototype at MIT Lincoln Laboratory

M. S. Hibbs\*  
R. R. Kunz

1994 IEEE Lithography  
Workshop,  
Quebec City, Canada,  
29 August–1 September 1994

---

\*Author not at Lincoln Laboratory.

<sup>†</sup>Titles of presentations are listed for information only. No copies are available for distribution.

193-nm Lithography	R. R. Kunz M. W. Horn C. L. Keast S. C. Palmateer M. Rothschild D. C. Shaver	1994 IEEE Lithography Workshop, Quebec City, Canada, 29 August–1 September 1994
Low-Power Charge-Domain Processing	A. M. Chiang	IEEE Signal Processing Society Chapter Meeting, Lexington, Massachusetts, 13 September 1994
Diamond Field-Emission Cathodes	M. W. Geis J. C. Twichell M. B. Stern N. N. Efremow K. E. Krohn T. M. Lyszczarz R. Uttaro	Lincoln Laboratory Technical Seminar Series, University of North Carolina, Raleigh, North Carolina, 13 September 1994
193-nm Optical Lithography: Current Status and Mask Requirements	D. C. Shaver	14th Annual Bay Area Chrome Users Society Symposium: Photomask Technology and Management, Santa Clara, California, 16 September 1994
Biochips: Microelectromechanical Systems for Molecular Biology	D. J. Ehrlich	Genome Sequencing and Analysis Conference, Hilton Head, South Carolina, 17-21 September 1994
Fabrication and Performance of $\text{In}_{0.53}\text{Ga}_{0.47}\text{As}/\text{AlAs}$ Resonant Tunneling Diodes Grown on GaAs Substrates	K. B. Nichols E. R. Brown M. J. Manfra O. B. McMahon	21st International Symposium on Compound Semiconductors, San Diego, California, 18-22 September 1994

193 nm — Moderately Extreme  
Ultraviolet

M. Rothschild

Extreme Ultraviolet  
Lithography Topical Meeting,  
Monterey, California,  
19-21 September 1994

Diamond Field-Emission Cathodes

M. W. Geis  
J. C. Twichell  
M. B. Stern  
N. N. Efremow  
K. E. Krohn  
T. M. Lyszczarz  
R. Uttaro

Diamond Films '94,  
Il Cioco, Italy,  
25-30 September 1994

Microchip Lasers

J. J. Zayhowski

1994 Optical Society  
of America Annual Meeting  
and Interdisciplinary Laser  
Science Conference,  
Dallas, Texas,  
2-7 October 1994

Nonlinear Surface Impedance:  
Measurements, Modelling and  
Effects in Devices

D. E. Oates

3rd Symposium on High  
Temperature Superconductors  
in High Frequency Fields,  
Cologne, Germany,  
3 October 1994

Development of Laser Systems for  
Atmospheric Adaptive Optics

T. H. Jeys

Lincoln Laboratory  
Technical Seminar Series,  
Rice University,  
Houston, Texas,  
5 October 1994

Wideband CO<sub>2</sub>-Laser Heterodyne  
Detection with GaAs/AlGaAs  
Multiple-Quantum-Well Structures

E. R. Brown  
K. A. McIntosh  
K. B. Nichols  
M. J. Manfra  
H. C. Liu  
G. E. Jenkins

186th Meeting of the  
Electrochemical Society:  
Symposium on Infrared  
Detectors,  
Miami, Florida,  
9 October 1994



InAsSb/AlAsSb Double-Heterostructure and InAsSb/InAlAs Quantum-Well Diode Lasers Emitting at $\sim 4\ \mu\text{m}$	H. K. Choi G. W. Turner Z. L. Liao	14th IEEE International Semiconductor Laser Conference, Maui, Hawaii, 10-12 October 1994
Growth of InAsSb Quantum Wells for Long Wavelength ( $> 4\ \mu\text{m}$ ) Lasers	G. W. Turner H. K. Choi H. Q. Le	North American Conference on Molecular Beam Epitaxy, Urbana, Illinois, 10-12 October 1994
Low-Power FIR Filter	A. M. Chiang J. R. LaFranchise M. M. Seaver	1994 Symposium on Low Power Electronics, San Diego, California, 10-12 October 1994
Overview of GaSb-Based Materials Research at MIT Lincoln Laboratory	G. W. Turner	Lincoln Laboratory Technical Seminar Series, Northwestern University, Evanston, Illinois, 14 October 1994
YBCO Thin Films for Microwave Applications	A. C. Anderson R. L. Slattery	Applied Superconductivity Conference, Boston, Massachusetts, 16-21 October 1994
YBCO/Ferrite Low-Loss Microwave Phase Shifter	G. F. Dionne D. E. Oates D. H. Temme	
Two-GHz Microstrip Thin-Film Resonators of Nb and $\text{YBa}_2\text{Cu}_3\text{O}_7$	J. D. Goettee* W. J. Skocpol* P. M. Mankiewich* D. E. Oates	

---

\*Author not at Lincoln Laboratory.

High-Power HTS Microstrip Filters for  
Cellular Base-Station Applications

G. C. Liang\*  
D. Zhang\*  
C.-F. Shih\*  
R. S. Withers\*  
M. E. Johansson\*  
W. Ruby\*  
B. F. Cole\*  
M. Krivoruchko\*  
D. E. Oates  
A. C. Anderson

Accuracy in High-Performance HTS  
Microwave Devices

W. G. Lyons  
A. C. Anderson  
L. H. Lee\*  
E. M. Macedo  
P. G. Murphy  
R. L. Slattery  
D. J. Baker

Nonlinear Microwave Surface Impedance  
in  $\text{YBa}_2\text{Cu}_3\text{O}_{7-x}$  Thin Films

D. E. Oates  
P. P. Nguyen\*  
G. Dresselhaus\*  
M. S. Dresselhaus\*

Niobium Superconducting Circuits  
for a 2-Gigachip-per-Second Spread-  
Spectrum Modem

J. P. Sage  
R. W. Ralston

Superconducting Cueing Receiver for  
Space Applications

T. C. L. G. Sollner  
W. G. Lyons  
D. R. Arsenault  
A. C. Anderson  
M. M. Seaver  
R. R. Boisvert  
R. L. Slattery

A Josephson-Junction Bridge Track-and-  
Hold Circuit

K. Y. Tam\*  
J. P. Sage

Applied Superconductivity  
Conference,  
Boston, Massachusetts,  
16-21 October 1994

---

\*Author not at Lincoln Laboratory.

GaSb-Based Diode Lasers for 2- to 5- $\mu$ m  
Emission

H. K. Choi

Lincoln Laboratory  
Technical Seminar Series,  
University of Massachusetts,  
Amherst, Massachusetts,  
20 October 1994

Integrated Optics

L. M. Johnson

Lincoln Laboratory  
Technical Seminar Series,  
University of Rochester,  
Rochester, New York,  
21 October 1994

Applications and Characterization  
of a New Face-Centered-Cubic  
Photonic Crystal

K. Agi  
E. R. Brown  
C. Dill III  
K. A. McIntosh  
O. B. McMahon  
K. M. Molvar  
K. J. Malloy

International Symposium on  
Guided-Wave Optoelectronics:  
Device Characterization,  
Analysis and Design,  
Brooklyn, New York,  
26-28 October 1994

Analysis of  $N \times M$  Waveguide Splitters  
and Couplers with Multimode  
Guiding Section

E. Thoen\*  
L. Molter\*  
J. P. Donnelly

Tensile-Strained AlGaAs/GaAsP  
Single-Quantum-Well Lasers

F. Agahi\*  
A. Baliga\*  
K. M. Lau\*  
H. K. Choi  
N. Anderson\*

Tunable Ytterbium Lasers

R. Allen\*  
L. Esterowitz\*  
T. Y. Fan

IEEE Lasers and Electro-Optics  
Society Annual Meeting,  
Boston, Massachusetts,  
31 October–3 November 1994

Application of Smart-Pixel and  
Microlens Arrays to Early Vision

B. F. Aull  
Z. L. Liao  
P. A. Maki  
E. R. Brown

Optical Analog Link Using a Linearized  
Modulator

G. E. Betts  
F. J. O'Donnell

---

\*Author not at Lincoln Laboratory.

Hybrid Devices and Packaging

J. P. Donnelly

Nondegenerate Four-Wave Mixing  
Wavelength Conversion in Low-Loss  
Passive InGaAsP/InP Waveguides

J. P. Donnelly  
H. Q. Le  
E. A. Swanson  
S. H. Groves  
A. Darwish\*  
E. P. Ippen\*

Mass-Transported Efficient Microlenses  
in GaAs and GaP for Integration with  
High-Power Diode Lasers

Z. L. Liao  
J. N. Walpole  
D. E. Mull  
D. L. Hovey  
W. F. DiNatale

Femtosecond Studies of Spectral Hole  
Burning in Semiconductor Lasers

C.-K. Sun\*  
B. Golubovic\*  
H. K. Choi  
C. A. Wang  
G. D. Sanders\*  
C. J. Stanton\*  
J. G. Fujimoto\*

High-Speed High-Density Parallel  
Free-Space Optical Interconnections

D. Z. Tsang  
H. V. Roussel  
J. D. Woodhouse  
J. P. Donnelly  
C. A. Wang  
D. L. Spears  
R. J. Bailey  
D. E. Mull

Single Layer Resists with Enhanced Etch  
Resistance for 193 nm Lithography

R. D. Allen\*  
G. M. Wallraff\*  
R. A. DiPietro\*  
D. C. Hofer\*  
R. R. Kunz

IEEE Lasers and Electro-Optics  
Society Annual Meeting,  
Boston, Massachusetts,  
31 October–3 November 1994

International Symposium on  
Photopolymers,  
Ellenville, New York,  
31 October–3 November 1994

---

\*Author not at Lincoln Laboratory.

## ORGANIZATION

### SOLID STATE DIVISION

D. C. Shaver, *Head*  
I. Melngailis, *Associate Head*  
J. F. Goodwin, *Assistant*  
  
A. L. McWhorter, *Division 8 Fellow*  
D. J. Ehrlich, *Senior Staff*  
E. Stern, *Senior Staff*  
C. L. Keast, *Staff*  
  
T. M. Bloomstein, *Research Assistant*  
J. T. Chiou, *Research Assistant*  
A. C. Hong, *Research Assistant*  
J. P. Mattia, *Research Assistant*  
N. L. DeMeo, Jr., *Associate Staff*  
J. W. Caunt, *Assistant Staff*  
K. J. Challberg, *Administrative Staff*

### SUBMICROMETER TECHNOLOGY

M. Rothschild, *Leader*  
T. M. Lyszczarz, *Assistant Leader*  
L. H. Dubois, *Senior Staff*

Astolfi, D. K.	Horn, M. W.
Craig, D. M.	Kunz, R. R.
DiNatale, W. F.	Maki, P. A.
Doran, S. P.	Palmateer, S. C.
Efremow, N. N., Jr.	Sedlacek, J. H. C.
Forte, A. R.	Stern, M. B.
Geis, M. W.	Twichell, J. C.
Goodman, R. B.	Uttaro, R. S.
Hartney, M. A.	

### QUANTUM ELECTRONICS

A. Sanchez-Rubio, *Leader*  
T. Y. Fan, *Assistant Leader*

Aggarwal, R. L.	Jeys, T. H.
Cook, C. C.	Kelley, P. L. <sup>‡</sup>
Daneu, V.	Le, H. Q.
DeFeo, W. E.	Ochoa, J. R.
DiCecca, S.	Zayhowski, J. J.
Dill, C., III	

### ELECTRONIC MATERIALS

B-Y. Tsaur, *Leader*  
D. L. Spears, *Assistant Leader*

Chen, C. K.	Krohn, L., Jr.
Choi, H. K.	Manfra, M. J.
Connors, M. K.	McGilvary, W. L.
Fahey, R. E. <sup>†</sup>	Nitishin, P. M.
Finn, M. C.	Pantano, J. V.
Golovchenko, P. A.	Paul, S. A.*
Harman, T. C.	Reinold, J. H., Jr.
Herrmann, F. P.	Turner, G. W.
Iseler, G. W.	Wang, C. A.

### HIGH SPEED ELECTRONICS

M. A. Hollis, *Leader*  
E. R. Brown, *Assistant Leader*  
R. A. Murphy, *Senior Staff*

Bozler, C. O.	McIntosh, K. A.
Chen, C. L.	McMahon, O. B.
Goodhue, W. D.	Molnar, R. J.
Harris, C. T.	Nichols, K. B.
Lincoln, G. A., Jr.	Rabe, S.
Mahoney, L. J.	Rathman, D. D.
Mathews, R. H.	

---

\* Research Assistant

<sup>†</sup> Part Time

<sup>‡</sup> Leave of Absence

## ELECTROOPTICAL DEVICES

R. C. Williamson, *Leader*  
L. M. Johnson, *Assistant Leader*

Aull, B. F.  
Bailey, R. J.  
Betts, G. E.  
Donnelly, J. P.  
Groves, S. H.  
Hovey, D. L.  
Liau, Z. L.  
Lind, T. A.  
Missaggia, L. J.

Mull, D. E.  
O'Donnell, F. J.  
Palmacci, S. T.  
Reeder, R. E.  
Roussell, H. V.  
Tsang, D. Z.  
Walpole, J. N.  
Woodhouse, J. D.

## ANALOG DEVICE TECHNOLOGY

R. W. Ralston, *Leader*  
T. C. L. G. Sollner, *Assistant Leader*  
A. C. Anderson, *Senior Staff*  
A. M. Chiang, *Senior Staff*

Arsenault, D. R.  
Boisvert, R. R.  
Brogan, W. T.  
Denneno, J. M.  
Feld, D. A.  
Fitch, G. L.  
Gleason, E. F.  
Holtham, J. H.  
LaFranchise, J. R.

Lyons, W. G.  
Macedo, E. M., Jr.  
McClure, D. W.  
Murphy, P. G.  
Oates, D. E.  
Sage, J. P.  
Seaver, M. M.  
Slattery, R. L.

## MICROELECTRONICS

E. D. Savoye, *Leader*  
B. B. Kosicki, *Assistant Leader*  
B. E. Burke, *Senior Staff*

Clark, H. R., Jr.  
Daniels, P. J.  
Doherty, C. L., Jr.  
Dolat, V. S.  
Donahue, K. G.  
Donahue, T. C.

Felton, B. J.  
Gregory, J. A.  
Hotaling, T. C.  
Johnson, K. F.  
Loomis, A. H.  
McGonagle, W. H.

Mountain, R. W.  
Percival, K. A.  
Reich, R. K.  
Thomas, J. W.<sup>§</sup>  
Young, D. J.

---

<sup>§</sup>Staff Associate

## 1. ELECTROOPTICAL DEVICES

### 1.1 TWO-SIDED ANAMORPHIC MICROLENS FOR COMPACT HIGH-POWER DIODE LASER SYSTEM

A novel two-sided anamorphic microlens has been fabricated by mass transport and is capable of coupling the astigmatic output of high-power tapered diode lasers [1]–[3] directly into a single-mode fiber. A high level of fiber-coupled power of 347 mW at 980-nm wavelength has been obtained, which demonstrates a new capability for miniaturizing high-power fiber-coupled diode laser systems [4].

Figure 1-1 illustrates the lens. The side facing the laser is close to cylindrical and is accurately designed using optical path-length considerations to remove the astigmatism by magnifying the source in the direction perpendicular to the junction plane. The effective aperture in that direction is  $\sim 150\text{ }\mu\text{m}$  and is positioned at  $127\text{ }\mu\text{m}$  from the laser facet. The side facing the fiber is close to spherical and is accurately designed to focus the beam to a spot comparable to the fiber mode diameter.

Microlenses were fabricated in a GaP substrate by single-step etching of multimesa preforms, which were subsequently smoothed by mass transport [5],[6]. In the lithographic pattern definition the two sides were readily aligned through the transparent substrate with the aid of registration marks. The mesas were formed by ion-beam-assisted  $\text{Cl}_2$  etching. After cleaning and light chemical etching, mass transport was carried out at  $1100^\circ\text{C}$  for 20 h in  $\text{PH}_3$  (2%) and Ar flow, in which sapphire plates were used for close wafer protection to prevent thermal etching and contamination.

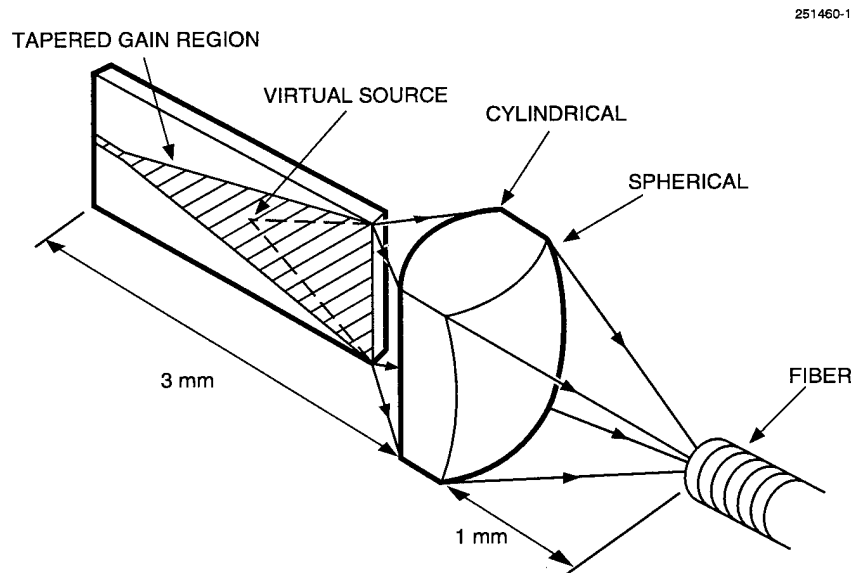


Figure 1-1. Schematic of present two-sided anamorphic microlens, which couples output from high-power tapered laser directly to single-mode fiber.

Figure 1-2 shows an optical micrograph of a fabricated lens array wafer viewed from the cylindrical lens side. Each lens appears as a pair of dark bands. The spherical lenses on the back side are seen as gray discs. Stylus profiles of the spherical and cylindrical lens surfaces are shown in Figure 1-3 and are in close agreement with design.

The microlens wafer was antireflection coated on both sides with evaporated  $\text{SiO}_x$  and was mounted on a specially designed micromanipulator stage capable of precisely aligning the lens to a tapered high-power laser to produce a tightly focused beam spot. Magnified images of the focused spot similar to the ones in Figure 1-4 show symmetric oval shapes with dimensions of 6.0 and 9.7  $\mu\text{m}$  in the directions parallel and perpendicular to the junction plane, respectively. This spot size is in close agreement with design and is suitable for efficient coupling to single-mode fiber.

The power coupled into a single-mode fiber with a mode field diameter of 7.1  $\mu\text{m}$  was measured to be 347 mW, which was 23% of the total laser output, as measured by a large-area detector placed close to the laser facet. When the laser was driven at a lower current, a somewhat higher coupling efficiency of 24.3% was measured with 227 mW in the fiber. It is worth noting that the total facet-to-fiber coupling efficiencies measured here include the microlens collection and transmission efficiencies as well as the mode matching to the fiber.

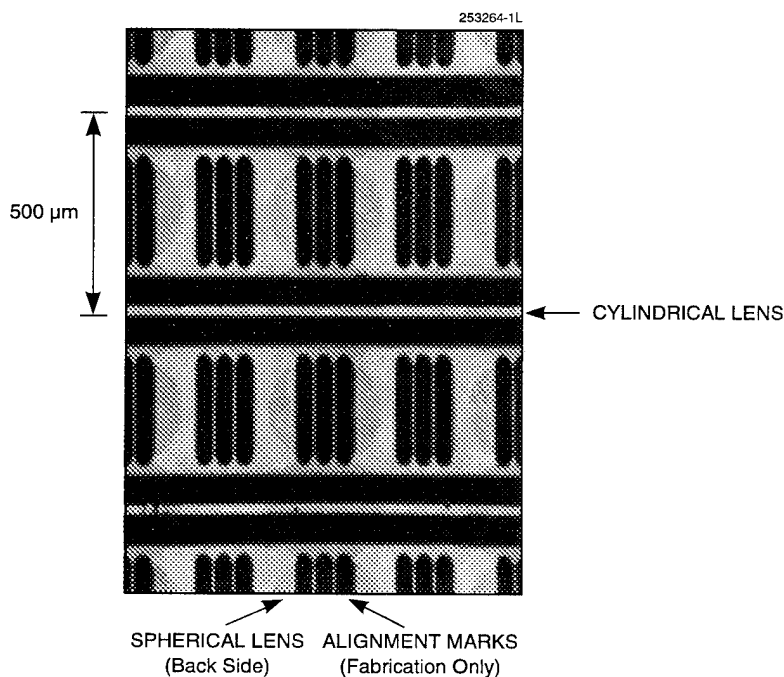


Figure 1-2. Optical micrograph of fabricated two-sided microlens wafer viewed from cylindrical lens side. The spherical lenses on the back side can also be seen through the transparent GaP substrate.



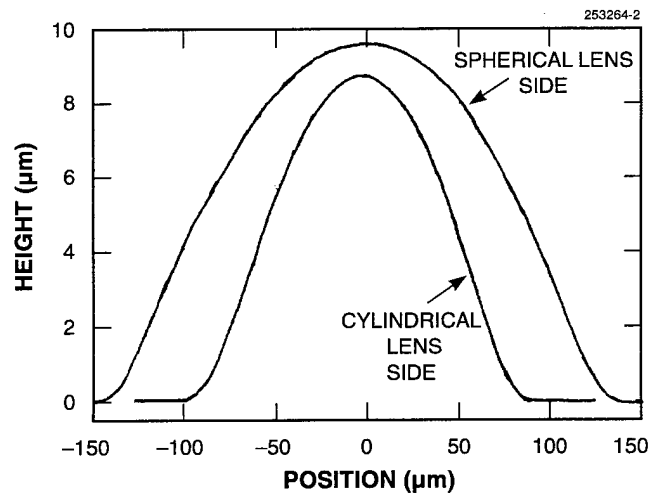


Figure 1-3. Stylus surface profiles of spherical and cylindrical sides of microlens.

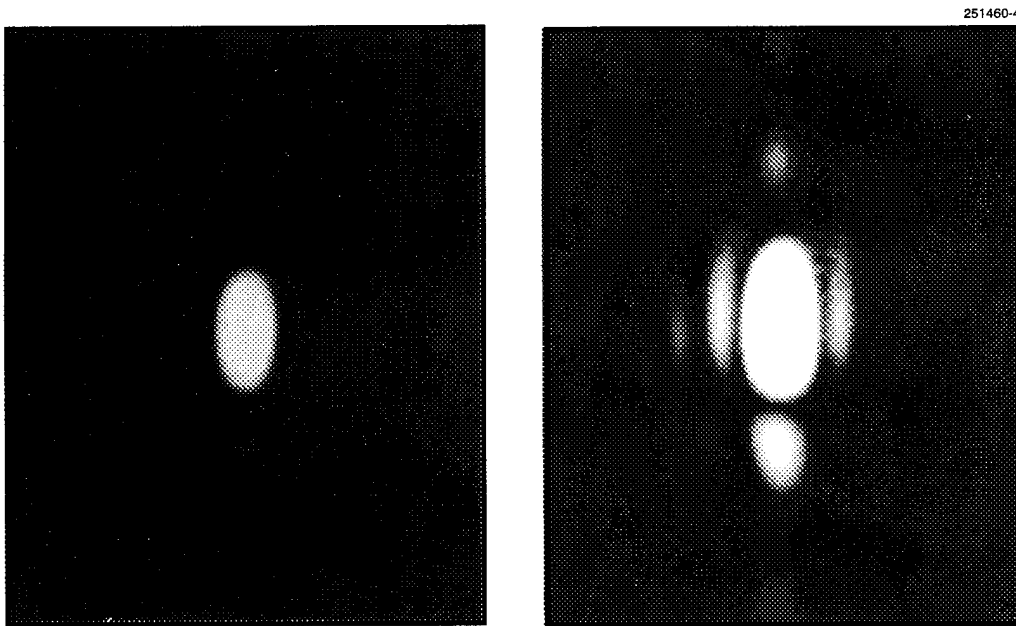


Figure 1-4. High-power tapered-laser output focused by two-sided anamorphic microlens. The overexposed photograph on the right shows some diffraction sidelobes.

Higher coupling efficiency and higher power can probably be achieved after more detailed evaluation and optimization of the microlens, the laser output, and the fiber coupling. The focused beam spot can be made more nearly round by further development of the microlens fabrication technology.

Z. L. Liao	D. E. Mull
J. N. Walpole	L. J. Missaggia
J. C. Livas	W. F. DiNatale

## REFERENCES

1. J. N. Walpole, E. S. Kintzer, S. R. Chinn, C. A. Wang, and L. J. Missaggia, *Appl. Phys. Lett.* **61**, 740 (1992).
2. E. S. Kintzer, J. N. Walpole, S. R. Chinn, C. A. Wang, and L. J. Missaggia, *IEEE Photon. Technol. Lett.* **5**, 605 (1993).
3. D. Mehuys, D. F. Welch, and L. Goldberg, *Electron. Lett.* **28**, 1944 (1992).
4. J. C. Livas, S. R. Chinn, E. S. Kintzer, J. N. Walpole, C. A. Wang, and L. J. Missaggia, *IEEE Photon. Technol. Lett.* **6**, 422 (1994).
5. Z. L. Liao, D. E. Mull, C. L. Dennis, R. C. Williamson, and R. G. Waarts, *Appl. Phys. Lett.* **64**, 1484 (1994).
6. Z. L. Liao, J. N. Walpole, D. E. Mull, C. L. Dennis, and L. J. Missaggia, *Appl. Phys. Lett.* **64**, 3368 (1994).

## 2. QUANTUM ELECTRONICS

### 2.1 COUPLED-CAVITY ELECTROOPTICALLY $Q$ -SWITCHED Nd:YVO<sub>4</sub> MICROCHIP LASERS

Prior to this work, coupled-cavity electrooptically  $Q$ -switched Nd:YAG microchip lasers had demonstrated the shortest  $Q$ -switched pulses (270 ps) and the highest rate of repetitive  $Q$  switching (500 kHz) reported for a solid state laser [1]. They had also produced the highest peak power (25 kW) obtained from any laser pumped by a single laser diode. However, Nd:YAG is not the best gain medium for these devices. In this work, we use a Nd:YVO<sub>4</sub> gain element in a coupled-cavity electrooptically  $Q$ -switched microchip laser.

The advantages of Nd:YVO<sub>4</sub> are a larger absorption coefficient  $\alpha$  (41 cm<sup>-1</sup> for Nd:YVO<sub>4</sub>, 12 cm<sup>-1</sup> for Nd:YAG), a larger gain cross section  $\sigma$  ( $1.6 \times 10^{-18}$  cm<sup>2</sup> for Nd:YVO<sub>4</sub>,  $3.3 \times 10^{-19}$  cm<sup>2</sup> for Nd:YAG), and a larger  $\sigma\tau$  product ( $1.6 \times 10^{-22}$  cm<sup>2</sup> s for Nd:YVO<sub>4</sub>,  $7.6 \times 10^{-23}$  cm<sup>2</sup> s for Nd:YAG), where  $\tau$  is the spontaneous lifetime of the gain medium [2]. All of these properties result in a larger intracavity small-signal round-trip gain  $G_{rt}$  for a given amount of incident pump power. This reduces the minimum possible duration  $t_w$  of a  $Q$ -switched pulse [3]:

$$t_w = \frac{8.1t_{rt}}{g_{rt}}, \quad (2.1)$$

where  $t_{rt}$  is the round-trip time of light within the laser cavity and  $g_{rt} \equiv \ln(G_{rt})$  is the round-trip gain coefficient when the pulse begins to form. Additionally, the larger absorption coefficient results in more efficient devices.

A coupled-cavity electrooptically  $Q$ -switched microchip laser consists of a Fabry-Perot gain cavity sharing a common mirror with an electrooptically tunable Fabry-Perot etalon, as illustrated in Figure 2-1. The principle behind the operation of the device is that the electrooptic etalon (defined by the two mirrors adjacent to the electrooptic material) serves as a variable-reflectivity output coupler for the gain cavity (defined by the two mirrors adjacent to the gain medium). The potential lasing modes of the device are determined primarily by the gain cavity. In the low- $Q$  state the etalon has a high transmission for all potential lasing modes so that none can reach threshold. In the high- $Q$  state the reflectivity of the etalon is high for the desired mode, and a  $Q$ -switched output pulse develops. To assure that all potential modes of the gain cavity can be simultaneously suppressed, the optical length of the etalon must be nearly an integral multiple of the optical length of the gain cavity. The higher the  $Q$  of the etalon, the tighter the tolerance on length. For an isotropic gain medium such as Nd:YAG, the length tolerance imposes a restriction on the birefringence of the electrooptic material, since oscillation must be suppressed for modes of both polarizations. This restriction is relaxed for anisotropic material, such as Nd:YVO<sub>4</sub>, where the gain for one polarization is larger than the gain for the other.

The minimum pulse width of a  $Q$ -switched system is obtained when the output coupling coefficient  $\gamma_o \equiv -\ln(1 - \Gamma_o)$ , where  $\Gamma_o$  is the total output coupling, is selected so that [3]

$$\gamma_o = 0.32g_{rt} - \gamma_{rt,p} \quad (2.2)$$

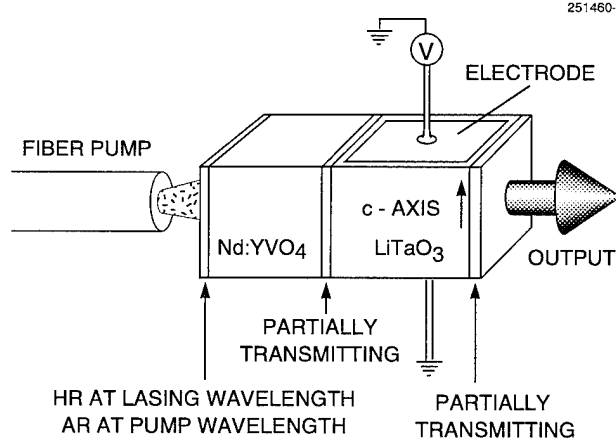


Figure 2-1. Coupled-cavity electrooptically *Q*-switched microchip laser (HR, highly reflecting; AR, antireflecting).

In this expression,  $\gamma_{rt,p} \equiv -\ln(1 - \Gamma_{rt,p})$  is the round-trip parasitic loss coefficient, where  $\Gamma_{rt,p}$  is the round-trip parasitic loss. Before Equation (2.2) can be used with the coupled-cavity microchip laser we must have an expression for the effective output coupling. Similarly, before Equation (2.1) can be used to determine the minimum pulse width of a coupled-cavity microchip laser we must have an expression for the effective round-trip time of the laser cavity.

The transmission of the electrooptic etalon is dynamically dependent on the rate of formation and decay of the pulse. For example, if the gain cavity and the etalon have the same optical length, the light within the gain cavity is amplified by the round-trip gain of the cavity before it is recombined with light that is reflected from the far mirror of the etalon. As a result, the effective transmission of a lossless etalon as seen at the interface between the gain medium and the etalon during the early formation of the pulse is

$$T_{et,t=0} = \frac{(1 - R_1)[1 - R_2 \exp(-m_l g_{rt})]}{1 + R_1 R_2 \exp(-m_l g_{rt}) - 2 \cos(\phi) \sqrt{R_1 R_2} \exp(-m_l g_{rt} / 2)} \quad , \quad (2.3)$$

where  $R_1$  is the reflectivity of the interface between the gain medium and the electrooptic material,  $R_2$  is the reflectivity of the output mirror on the etalon,  $m_l = t_{rt,et}/t_{rt,g}$  is the ratio of the round-trip time of light in the etalon  $t_{rt,et}$  to the round-trip time of light in the gain cavity  $t_{rt,g}$ , and  $\phi = 2\pi(t_{rt,et} - t_{rt,g})\nu_o$ , with  $\nu_o$  being the oscillating frequency of the laser. In order to hold off lasing we must be able to satisfy the relationship

$$T_{et,t=0} \geq 1 - \exp(\gamma_{rt,p} - g_{rt}) \quad . \quad (2.4)$$

Near the peak of the output pulse the gain of the laser is saturated and the effective transmission of the etalon approaches its CW transmission

$$T_{\text{et,cw}} = \frac{(1-R_1)(1-R_2)}{1+R_1R_2-2\cos(\phi)\sqrt{R_1R_2}} \quad (2.5)$$

Since the pulse width of the laser is determined by the transmission of the etalon near the peak, it is this value of transmission that should be used as the output coupling  $\Gamma_o$  in Equation (2.2).

The transit time of light in the etalon affects the behavior of the coupled-cavity  $Q$ -switched laser in a second way. After leaving the gain cavity, light must escape the etalon, which has an associated decay time. In order to minimize this effect and reduce the pulse width it is desirable to keep  $R_2$  as small as possible. The minimum pulse width is therefore obtained by selecting values of  $R_1$  and  $R_2$  that satisfy the equations

$$\frac{(1-R_1)[1-R_2\exp(-m_l g_{\text{rt}})]}{1+R_1R_2\exp(-m_l g_{\text{rt}})-2\sin(2\pi\nu_o\delta_1)\sqrt{R_1R_2}\exp(-m_l g_{\text{rt}}/2)} = 1 - \exp(\gamma_{\text{rt,p}} - g_{\text{rt}}) \quad (2.6)$$

$$\frac{(1-R_1)(1-R_2)}{1+R_1R_2+2\sin(2\pi\nu_o\delta_2)\sqrt{R_1R_2}} = 1 - \exp(\gamma_{\text{rt,p}} - 0.32g_{\text{rt}}) \quad (2.7)$$

where  $\delta_1 + \delta_2 = \delta(t_{\text{rt,et}})$  is the total change in the round-trip time of the electrooptic etalon induced during  $Q$  switching and the amount of change associated with  $\delta_1$  and  $\delta_2$  is determined by the exact optical length of the etalon before  $Q$  switching.

For low-gain operation ( $g_{\text{rt}} \ll 1$ ), the solution to Equations (2.6) and (2.7) yields a high value for  $R_1$  and a low value for  $R_2$ , and the effective round-trip time of a properly optimized coupled-cavity laser is approximately the round-trip time of the gain cavity. In very high gain systems,  $R_2$  becomes larger than  $R_1$  and the effective round-trip time of the coupled cavity approaches the sum of the round-trip times of the gain cavity and the etalon. A simple expression that satisfies these asymptotic constraints and has a reasonable fit to numerical simulations is

$$t_{\text{rt}} = t_{\text{rt,g}} \left[ 1 + \frac{m_l(\gamma_{\text{rt,p}} - 0.32g_{\text{rt}})}{\ln(R_2)} \right] \quad (2.8)$$

Figure 2-2 shows the resulting normalized effective round-trip time of an optimized coupled-cavity laser with  $\delta_1 = \delta_2 = 1/4\nu_o$  as a function of gain for  $m_l = 1$  and 2, for  $\gamma_{\text{rt,p}} = 0$ . Over a large part of the potential operating range of the coupled-cavity  $Q$ -switched laser the effective cavity length is the length of the gain cavity; the length of the  $Q$  switch does not contribute significantly.

Coupled-cavity electrooptically *Q*-switched microchip lasers were constructed from 440- $\mu\text{m}$ -long pieces of 1.1-wt% Nd:YVO<sub>4</sub> bonded to 900- $\mu\text{m}$ -long pieces of LiTaO<sub>3</sub>, as illustrated in Figure 2-1. Both materials were polished flat and parallel on the two faces normal to the cavity axis and oriented with their *c*-axes parallel to each other, orthogonal to the cavity axis. Electrodes were deposited on the faces of the LiTaO<sub>3</sub> normal to the *c*-axis with an electrode spacing of  $\sim 1$  mm. The pump-side faces of the Nd:YVO<sub>4</sub> were coated dielectrically to transmit the pump light and to be highly reflective at the oscillating wavelength (1.064  $\mu\text{m}$ ). Greater than 90% of the incident 808-nm pump light from a butt-coupled fiber was absorbed by the gain medium.

In one device, designed for low repetition rates and short output pulses, a partially transmitting mirror between the two materials had a reflectivity of 41% at 1.064  $\mu\text{m}$  and reflected the pump light. The output face of the LiTaO<sub>3</sub> was coated for 32% reflectivity at 1.064  $\mu\text{m}$ . *Q* switching was performed by applying a 960-V pulse with a 1.8-ns rise time to the LiTaO<sub>3</sub> at repetition rates up to 1 kHz. The temperature of the device was adjusted to control the relative optical lengths of the gain medium and electrooptic etalon. Under optimized conditions, lasing could be held off for a maximum incident CW pump power of 0.5 W. At this pump level the output pulses had an energy of 12  $\mu\text{J}$  and the pulse width observed on an oscilloscope was 129 ps. Deconvolution of the 60-ps detector impulse response results in an optical pulse width  $< 115$  ps, with a peak power of  $\sim 90$  kW. An oscilloscope trace of the pulse is shown in Figure 2-3. During *Q*-switched operation the laser was single frequency, linearly polarized, and near diffraction limited, with a 100- $\mu\text{m}$  waist.

A second *Q*-switched Nd:YVO<sub>4</sub> microchip laser was designed for operation at high repetition rates. This device was similar to the one just described, except that the partially transmitting mirror between the Nd:YVO<sub>4</sub> and the LiTaO<sub>3</sub> had a reflectivity of 97% at 1.064  $\mu\text{m}$  and the output face of the LiTaO<sub>3</sub> was coated for 50% reflectivity at 1.064  $\mu\text{m}$ . Temperature and a dc bias on the electrodes were used to minimize the duration of the output pulses. Pumped with 1.2 W of incident power, the average output power of the laser was 360 mW for all pulse repetition rates between 300 kHz and 2.25 MHz. As shown in Figure 2-4, the pulse

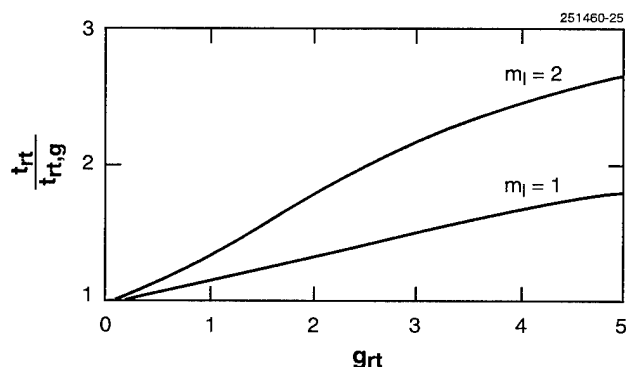


Figure 2-2. Effective cavity round-trip time vs gain for optimized coupled-cavity *Q*-switched laser with  $m_l = 1$  and  $m_l = 2$ .

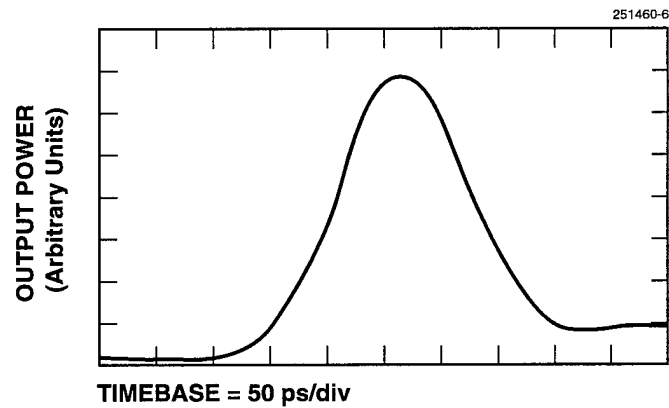


Figure 2-3. Oscilloscope trace of 115-ps pulse from coupled-cavity Q-switched Nd:YVO<sub>4</sub> microchip laser pumped with 0.5 W of incident CW diode power. The impulse response of the detector is 60 ps in duration; the afterpulse in the trace is the result of electrical ringing in the detector.

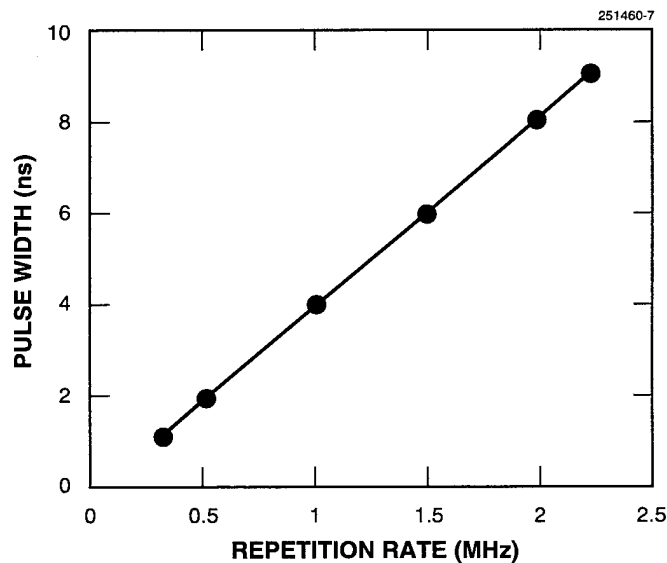


Figure 2-4. Pulse width as function of pulse repetition rate for coupled-cavity Q-switched Nd:YVO<sub>4</sub> microchip laser pumped with 1.2 W of incident CW diode power.

width increased linearly with pulse repetition rate, from 1.2 ns at 300 kHz to 8.8 ns at 2.25 MHz. At the highest pulse repetition rate (2.25 MHz) the energy per pulse was 0.16  $\mu\text{J}$  and the peak pulse power was 16 W. The laser was single frequency, linearly polarized, and near diffraction limited, with an 85- $\mu\text{m}$  waist at all repetition rates. The pulse-to-pulse amplitude jitter and timing jitter were measured to be  $< 0.5\%$  and  $< 0.5$  ns, respectively.

The coupled-cavity Nd:YVO<sub>4</sub> *Q*-switched microchip lasers outperform similar Nd:YAG devices and produce the shortest *Q*-switched pulses (115 ps) and the highest rate of repetitive *Q* switching (2.25 MHz) yet reported for a solid state laser. They also produce the highest peak power (90 kW) obtained from any laser pumped by a single laser diode. The geometry of the electrooptically *Q*-switched microchip lasers allows them to be produced inexpensively as individual devices or in one- and two-dimensional arrays. The complete device fits into a package approximately the size of a conventional diode laser package. Potential applications of the device include remote sensing, nonlinear frequency generation, micromachining, and microsurgery.

J. J. Zayhowski	C. Dill III
J. L. Daneu	C. Cook

## 2.2 THERMAL EVAPORATION OF LOW-IMPEDANCE Al-AlO<sub>x</sub>Pb JUNCTIONS

Normal metal-oxide superconducting junctions, which are used in studies of high-speed nonlinear response to light, must be fast enough to detect a difference frequency of  $\sim 1$  MHz [4]. For a junction area of  $20 \times 20 \mu\text{m}$  and capacitance of  $\sim 50$  pF [4], this implies a requirement of 3-k $\Omega$  junction impedance. A lower limit of 1 k $\Omega$  also exists because of minimum signal amplitude requirements. Previous attempts to fabricate such junctions utilizing a bell-jar thermal deposition process of aluminum with an intermediate atmospheric exposure (oxidation) for mask rotation and then sputter evaporation of lead resulted in junctions with an impedance of at least 10 k $\Omega$  and with poor stability, rising to effectively infinite impedance in just a couple of days [4].

The thickness of AlO<sub>x</sub> formed on the surface of freshly evaporated aluminum by oxygen exposure usually saturates at  $\sim 25 \text{ \AA}$  [5]. It can be shown that for a junction impedance of 1–3 k $\Omega$  a surface oxide between 10 and 15  $\text{ \AA}$  is required. Since junction impedance varies exponentially with oxide layer thickness it is important to be able to grow the oxide to a well-defined value. We chose an in-chamber oxygen exposure without a vacuum break as the method of forming the oxide layer. This thermal oxidation technique was selected because we believed the oxide thickness could be easily tailored by simply adjusting the exposure time. The impedance of the junctions was expected to vary exponentially with exposure time.

The junctions were fabricated in an electron-beam evaporation system with quartz-crystal thickness monitoring and rate control. The inside of the chamber, along with the substrates, was prebaked for 1 h with 4-kW radiant heaters, which typically resulted in substrate temperatures between 150 and 220°C. The substrates were then cooled to about 30°C.



Quartz substrates were attached to a water-traced copper slab mounted through the side of the chamber about 11.5 in. above the four-pocket electron-beam source. Each stripe of the junction was formed by coating through a mask in contact with the substrates. A mechanism was developed to allow changing the masks without breaking vacuum. The aluminum was deposited at a rate of 0.3 nm/s to a thickness of 20 nm. After evaporation of the aluminum the chamber was isolated from the vacuum pump, and commercial oxygen was bled in for a period of 5, 6, 8, or 10 min. The valve was then closed and the chamber returned to high vacuum, giving the exposure profiles shown in Figure 2-5. Despite the inference from the curves, in no case did the chamber ever reach atmospheric pressure. After oxidation and changing the mask, the lead contact was coated at a rate of 3.0 nm/s to a thickness of 0.5, 1.0, or 3.5  $\mu\text{m}$ . Both contacts were evaporated at a substrate temperature of about 20°C, and the pressure remained below  $5 \times 10^{-7}$  mbar.

About 20 fabrication processes were performed, each yielding six junctions. In each iteration the oxygen exposure time and lead layer thickness were varied in an attempt to improve the impedance and/or stability of the junctions. The average impedance of a given iteration was computed by averaging the impedance for each set of six junctions. Only the results of iterations with similar evaporation and oxidation conditions were compared.

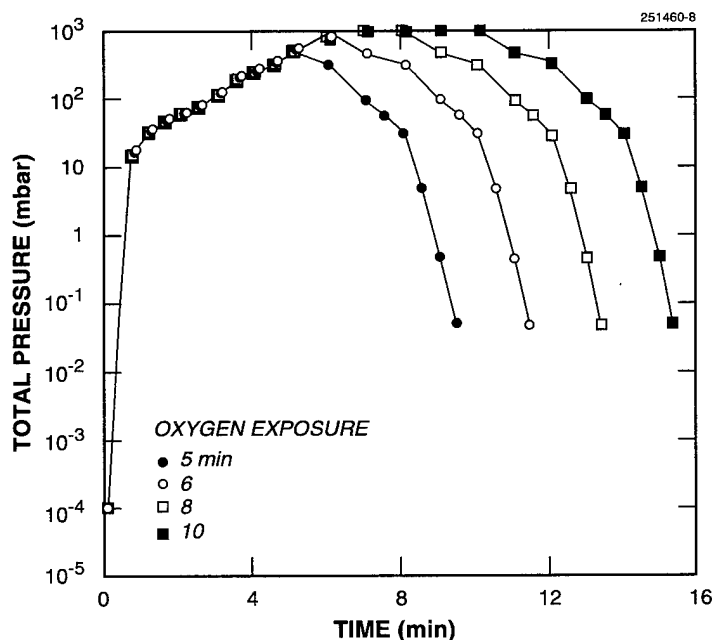


Figure 2-5. Oxygen exposure profiles for 5-, 6-, 8-, and 10-min. cycles used in junction fabrication process.

The dependence of the impedance on oxygen exposure time for junctions measured one day after fabrication is shown in Figure 2-6. As expected, the junction impedance was generally seen to increase with oxygen exposure, but the increase was not exponential. The reason for this is in the growth mechanism of thermally oxidized metals. In order to form an oxide film on a metal, oxygen must be present as well as an electric field of proper magnitude and sign across the forming oxide [6]. In the case of thermal oxidation a constant potential is supplied by adsorbed oxygen ions initially on the metal and later on the surface of the oxide. However, as the oxide film grows, the magnitude of the electric field at the metal/oxide interface decreases. This makes it more and more difficult for positive metal ions to migrate through the oxide and combine with oxygen at the surface, thereby slowing the growth rate of the oxide significantly more than we had expected. If a more detailed study could verify the linear dependence of impedance on exposure time at constant pressure, as shown in Figure 2-6, then the growth rate could be shown to decrease exponentially [4]. Based on this slow oxide formation mechanism, the previously developed process using bell-jar thermal evaporation should also have given relatively low impedance junctions. That it did not may be due to the effect reported by Miles and Smith [6], in which high junction impedances were believed to result from a contamination of the evaporating aluminum by water vapor in an unbaked chamber.

Interpolation of the impedance stability results for four sets of junctions is presented in Figure 2-7. The curves show clearly that a larger lead thickness resulted in improved stability owing to the passivation properties of the lead against migration of atmospheric oxygen into the junction. Since operation of these tunneling junctions involves biasing, impedance stability can also be disrupted by the effect of solid state oxidation [6] if the lead contact becomes oxidized during evaporation. The evaporative gettering of oxygen before the lead evaporation may therefore improve stability as well. Finally, the relative increase in impedance is seen to be greater for junctions with higher initial impedance, as in the case of  $Pb = 1000$  nm shown in Figure 2-7. This is probably because the junction impedance increases exponentially with the growing oxide layer after exposure to air.

In our experiments we found that low junction impedance depended mostly on the removal of water vapor from the chamber. The stability in impedance was shown to depend on lead contact thickness, while relative stability depended on the initial impedance of the junctions. A lead thickness of 1000 nm or greater was seen to reach a quasi-equilibrium impedance after about 20–30 days.

Future improvements would include better chamber/substrate baking and oxygen gettering techniques to help remove water vapor from the chamber before initiating the fabrication process. Cryogenic drying of the commercial oxygen or other methods of purifying the oxygen would also improve oxide formation homogeneity and lead contact purity.

C. Cook

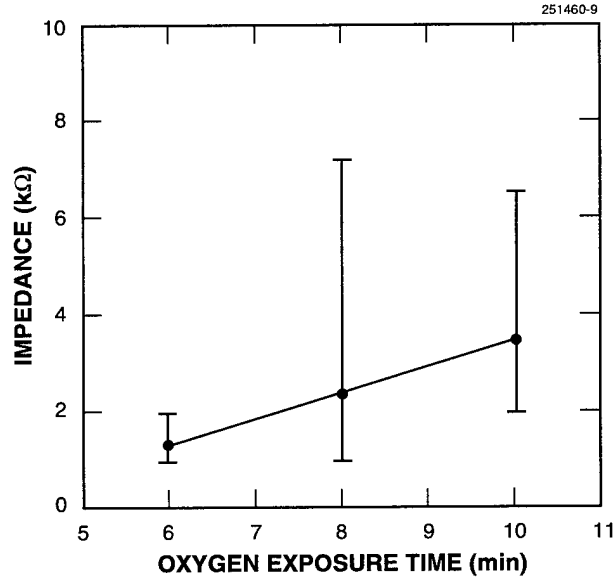


Figure 2-6. Junction impedance resulting from different exposure times, measured one day after fabrication. Only data from processes with similar parameters are plotted.

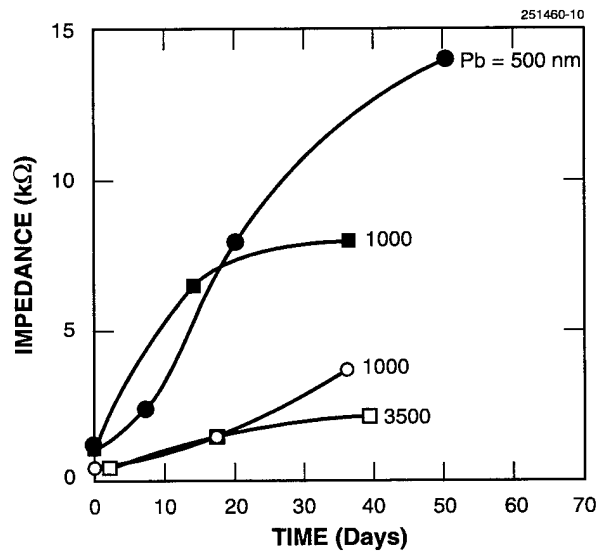


Figure 2-7. Impedance stability of junctions of differing lead contact thickness showing improved stability with thicker passivation and greater absolute increases resulting from junctions of higher starting impedance.

## REFERENCES

1. J. J. Zayhowski and C. Dill III, *Opt. Lett.* **17**, 1201 (1992).
2. R. A. Fields, M. Birnbaum, and C. L. Fincher, *Appl. Phys. Lett.* **51**, 1885 (1987).
3. J. J. Zayhowski and P. L. Kelley, *IEEE J. Quantum Electron.* **27**, 2220 (1991); **29**, 1239 (1993).
4. M. Otteson, private communication.
5. J. Verba and S. Woods, *Can. J. Phys.* **50**, 548 (1972).
6. J. Miles and P. Smith, *J. Electro-Chem. Soc.* **110**, 1240 (1963).

### 3. MATERIALS RESEARCH

#### 3.1. HIGH-POWER, HIGH-TEMPERATURE OPERATION OF GaInAsSb-AlGaAsSb RIDGE-WAVEGUIDE LASERS EMITTING AT 1.9 $\mu\text{m}$

Diode lasers emitting at  $\sim 2 \mu\text{m}$  have many potential applications such as in pumping Ho-doped solid state lasers emitting at  $2.1 \mu\text{m}$ , in tissue welding and surgery because of strong absorption in human tissue, and in spectroscopy. Quantum-well lasers incorporating compressively strained GaInAsSb active layers and AlGaAsSb barrier/confining layers grown on GaSb substrates have exhibited excellent room-temperature performance at  $\sim 2 \mu\text{m}$ . Pulsed threshold current density as low as  $143 \text{ A/cm}^2$  and single-ended CW output power as high as  $1.3 \text{ W}$  have been described [1]. Here, we report high-power GaInAsSb/AlGaAsSb ridge-waveguide lasers emitting at  $\sim 1.9 \mu\text{m}$ . Single-ended CW power as high as  $100 \text{ mW}$  has been obtained, which is the highest power achieved for any ridge-waveguide lasers emitting at  $\sim 2 \mu\text{m}$ . These devices have operated CW at temperatures up to  $130^\circ\text{C}$ .

The laser structure, grown on an  $n$ -GaSb substrate by molecular beam epitaxy, has the following layers:  $n^+$ -GaSb buffer,  $2\text{-}\mu\text{m}$ -thick  $n\text{-Al}_{0.85}\text{Ga}_{0.15}\text{As}_{0.07}\text{Sb}_{0.93}$  cladding, active region consisting of five  $10\text{-nm}$ -thick  $\text{Ga}_{1-x}\text{In}_x\text{As}_y\text{Sb}_{1-y}$  wells and six  $20\text{-nm}$ -thick  $\text{Al}_{0.25}\text{Ga}_{0.75}\text{As}_{0.02}\text{Sb}_{0.98}$  barriers,  $2\text{-}\mu\text{m}$ -thick  $p\text{-Al}_{0.85}\text{Ga}_{0.15}\text{As}_{0.07}\text{Sb}_{0.93}$  cladding, and  $0.05\text{-}\mu\text{m}$ -thick  $p^+$ -GaSb contacting. All the layers are nominally lattice matched to the substrate, except for the active well, which is under compressive strain of  $\sim 5 \times 10^{-3}$ . Based on the growth parameters and the amount of strain, the best estimate for the active layer composition is  $x=0.14$  and  $y=0.05$ . The compressive strain was found to reduce the threshold current density substantially. The pulsed threshold current density for a  $1\text{-mm}$ -long device is  $\sim 200 \text{ A/cm}^2$ .

The ridge-waveguide lasers were fabricated by the following process. First, a layer of  $\text{SiO}_2$  was deposited. Patterns for  $5\text{-}\mu\text{m}$ -wide ridges were defined by photolithography. The  $\text{SiO}_2$  was etched with buffered HF, and the photoresist was removed. Ridges were then formed by reactive ion etching in a  $\text{BCl}_3/\text{Ar}$  plasma. Next, the remaining  $\text{SiO}_2$  was removed and a new  $\text{SiO}_2$  layer was deposited. Contact openings were made on top of the ridges, and the wafer was metallized with Ti/Pt/Au for the  $p^+$  contact. The wafer was lapped to  $\sim 100 \mu\text{m}$  and the  $n$  GaSb was metallized with Au/Sn/Ti/Pt/Au, which was subsequently alloyed at  $300^\circ\text{C}$ .

For uncoated devices with cavity lengths  $L = 500$  and  $1000 \mu\text{m}$ , pulsed threshold currents at room temperature were about  $20$  and  $30 \text{ mA}$ , respectively. These values are substantially lower than the  $50$  and  $70 \text{ mA}$  reported for previous GaInAsSb/AlGaAsSb ridge-waveguide lasers with the same cavity lengths [2]. The reduction in threshold currents is due to a lower threshold current density of the laser structure ( $200$  vs  $300 \text{ A/cm}^2$  for  $L = 1000 \mu\text{m}$ ) and a narrower stripe width ( $5$  vs  $8 \mu\text{m}$ ). One device with  $L = 1000 \mu\text{m}$  was coated for high reflection ( $> 95\%$ ) on the back facet, and for passivation with  $15\text{-nm}$ -thick aluminum oxide on the front facet. The CW threshold current was  $30 \text{ mA}$  and the maximum power was  $50 \text{ mW}$  at  $450 \text{ mA}$ . The front facet of the device was then antireflection (AR) coated with  $\text{SiO}$  to have reflectivity  $< 1\%$ . Figure 3-1 shows the CW output power vs current for the AR-coated device at a heatsink temperature of  $20^\circ\text{C}$ . The threshold current is increased to  $40 \text{ mA}$  and the initial slope efficiency is  $0.25 \text{ W/A}$ , corresponding to a differential quantum efficiency of  $39\%$ . The maximum output power is  $100 \text{ mW}$  obtained at  $525 \text{ mA}$ , limited by the junction temperature rise. This power is substantially higher than the  $28 \text{ mW}$  reported previously for GaInAsSb/AlGaAsSb ridge-waveguide lasers [2] and the  $25 \text{ mW/facet}$  for InGaAs/InGaAsP ridge-waveguide lasers emitting at  $\sim 2 \mu\text{m}$  [3].

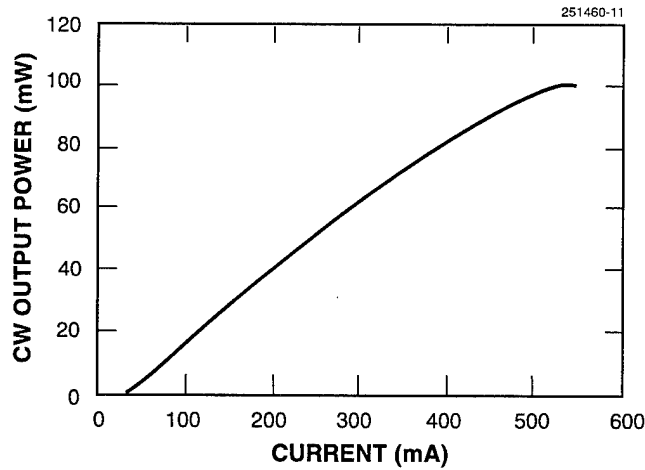


Figure 3-1. Output power vs current of 1000- $\mu\text{m}$ -long GaInAsSb/AlGaAsSb ridge-waveguide laser at 20°C. The front and back facets are coated to have reflectivity < 1% and > 95%, respectively.

The lateral far-field pattern maintained a single mode up to the maximum output power. The full width at half-maximum at low power levels is  $\sim 20^\circ$ , but gradually increases to  $\sim 25^\circ$  at high power levels. There was a slight shift of  $\sim 2^\circ$  in the peak position as the power was increased. Such an increase in the far-field angle and a shift in the peak position have been observed in other ridge-waveguide lasers emitting at shorter wavelengths, and have been attributed to a finite amount of gain guiding and relatively weak index guiding [4].

The emission spectra of the laser at low power levels show multiple longitudinal modes at  $\sim 1.92 \mu\text{m}$ . For power between 35 and 45 mW, however, the spectrum becomes predominantly a single longitudinal mode, as shown in Figure 3-2. The side mode suppression ratio is  $\sim 20$ . At higher power levels, two or three dominant modes are observed that are separated by  $\sim 50 \text{ nm}$ .

Figure 3-3 shows CW power vs current curves at several heatsink temperatures of another 1000- $\mu\text{m}$ -long device with high-reflection and passivation coatings on the back and front facets, respectively. For temperatures between 20 and 80°C, the characteristic temperature  $T_0$  is 85 K, which is significantly higher than the 48 K obtained for InGaAs/InGaAsP ridge-waveguide lasers emitting at  $\sim 2 \mu\text{m}$  [3]. The slope efficiency does not change appreciably between 20 and 60°C, but becomes smaller at higher temperatures. The maximum CW operating temperature is 130°C, which is 100°C higher than for GaInAsSb/AlGaAsSb double-heterostructure lasers [5].

H. K. Choi  
G. W. Turner  
M. K. Connors

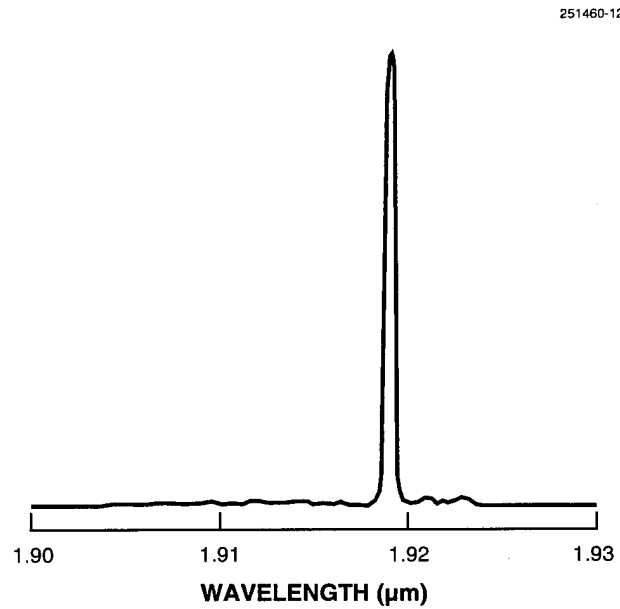


Figure 3-2. Emission spectrum of GaInAsSb/AlGaAsSb ridge-waveguide laser at CW power of 40 mW.

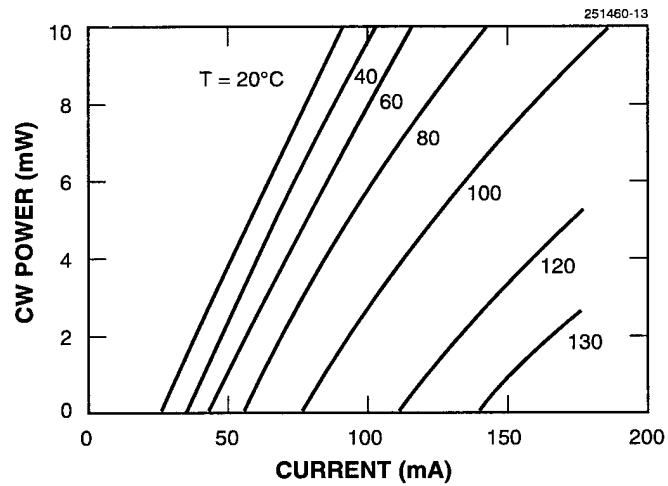


Figure 3-3. Output power vs current for CW operation of 1000- $\mu\text{m}$ -long GaInAsSb/AlGaAsSb ridge-waveguide laser at several heatsink temperatures.

## REFERENCES

1. H. K. Choi, G. W. Turner, and S. J. Eglash, *IEEE Photon. Technol. Lett.* **6**, 7 (1994).
2. H. K. Choi, S. J. Eglash, and M. K. Connors, *Appl. Phys. Lett.* **63**, 3271 (1993).
3. J. S. Major, Jr., D. W. Nam, J. S. Osinski, and D. F. Welch, *IEEE Photon. Technol. Lett.* **7**, 733 (1993).
4. J. Nappi, A. Ovtchinnikov, H. Aosen, P. Savolainen, and M. Pessa, *Appl. Phys. Lett.* **64**, 2203 (1994).
5. H. K. Choi and S. J. Eglash, *Appl. Phys. Lett.* **59**, 1165 (1991).



## 4. SUBMICROMETER TECHNOLOGY

### 4.1 INTEGRATED CIRCUIT INTERCONNECT TECHNIQUE FOR HIGH-DENSITY APPLICATIONS

Integrated circuits (ICs) typically use bond wires attached to 100- $\mu\text{m}$  pads to provide the electrical interconnect between the chip and the package or multichip module (MCM) substrate. Although this technique is simple and flexible, it is not well suited for high-performance, high-density connections. With more advanced techniques [1] such as taped automated bonding (TAB) or solder bump connections, the performance is improved, but the chips require special processing during IC fabrication. The limited availability of specialized chips for this purpose impacts the usefulness of the techniques, especially in low-volume and prototyping applications.

This report describes a novel high-density interconnect technique designed to accommodate standard commercially fabricated chips in die form. A 50- $\mu\text{m}$  interconnect pitch has been demonstrated, which is denser than typical TAB interconnect by a factor of 2. With further development the process could be scaled to a 20- $\mu\text{m}$  pitch.

Our approach is based on high-density platinum beam leads fabricated on the IC die, with matching high-density solder bumps fabricated on the MCM. The beam leads provide electrical contact to the bonding pads and a wettable surface for soldering, and they physically isolate the bonding pads from the solder thereby preventing contamination of the IC. Figure 4-1 illustrates a beam lead test pattern fabricated on an IC chip. It is possible to back-side etch the chips to form true cantilevered beams suspended on the passivation oxide. This approach simplifies the alignment of the chip to the MCM and also permits inspection of the interconnect after attachment. Alternatively, the processing can be simplified by eliminating the back-side etch and using an aligner/bonder designed for opaque substrates.

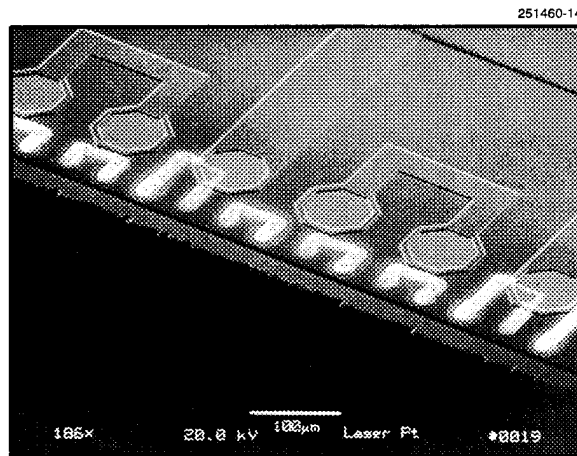


Figure 4-1. Scanning electron micrograph of platinum beam leads fabricated on integrated circuit chip. In this test pattern, the short U-shaped wires form a continuity structure when combined with the solder bumps and wiring on the multichip module (MCM) substrate. The long U-shaped wires provide contact to the bonding pads on the chip.

Conventional photolithographic techniques could be used to define beam leads on IC wafers, but are cumbersome when dealing with individual circuit die. We have used a laser direct-write system [2] to form the beam leads. This system can pattern metal in a one-step process without the use of photoresist or etching and can align to features on the chip. The platinum deposition process is based on the selective pyrolysis of  $\text{Pt}(\text{PF}_3)_4$  vapor at  $\sim 5$ -Torr pressure in a static cell using an  $\text{Ar}^+$  laser operated at 488 nm. A 50 $\times$ , 0.45-NA, long-working-distance objective is used to focus the beam to an  $\sim 1\text{-}\mu\text{m}$ -diam spot. The laser power at the focus is usually  $\sim 50$  mW. Writing rates of platinum are in the range  $\sim 250\text{ }\mu\text{m/s}$ , and can be as high as 5 mm/s on substrates such as polyimide. The resistivity of the deposited material is 10-11  $\mu\Omega\text{ cm}$ , and typical connections are 5  $\mu\text{m}$  wide and  $\sim 1\text{ }\mu\text{m}$  thick. The platinum wires exhibit good step coverage and form good electrical contact to the aluminum bond pads on the die, and the fabrication process does not seem to damage the underlying oxide.

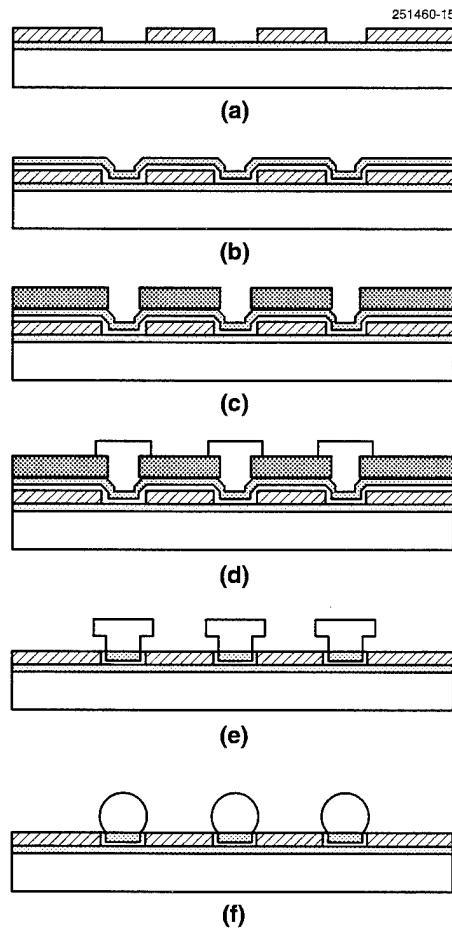


Figure 4-2. Solder bump fabrication processing steps: (a) MCM substrate, (b) titanium and copper deposited to form the under-bump metallization, (c) locations for solder bumps defined in photoresist, (d) electroplating of lead and tin, (e) stripping of photoresist, copper, and titanium (the solder bumps mask the removal of the copper and titanium on the pads), and (f) alloying the lead/tin aggregate to form the solder bumps.

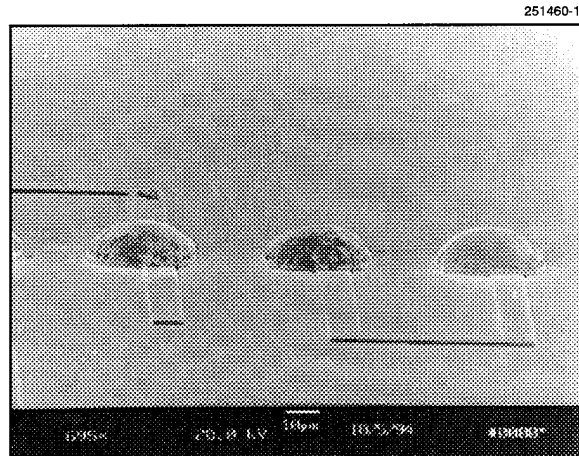


Figure 4-3. Scanning electron micrograph of solder bumps fabricated on MCM substrate.

After the platinum leads have been defined the cantilevered structures are fabricated by etching the underlying silicon. The IC is placed face down in a reactive ion etching system. The IC is suspended in the glow and etched for 20 min using 30 mTorr of  $\text{SF}_6$  at 200 W. Under these conditions the silicon on the sides of the IC are etched at  $1 \mu\text{m}/\text{min}$ , but the passivation oxide on the front surface and the platinum leads are not etched appreciably. The resulting structure comprises a silicon substrate with an overhanging  $\text{SiO}_2$  layer. The platinum beam leads extend to the end of this overhang.

The solder bumps are fabricated on the MCM with conventional IC processing techniques, as illustrated in Figure 4-2. The processing starts with a MCM substrate comprising a silicon wafer with aluminum metallization, an oxide passivation layer, and oxide openings over the bonding pads. The wafer is sputter cleaned to remove the native oxide from the aluminum pads, and  $200 \text{ \AA}$  of titanium followed by  $2000 \text{ \AA}$  of copper are then sputtered onto the sample. The titanium provides good electrical and mechanical contact to the aluminum surface, while the copper is compatible with the solder. Photoresist is then patterned to define the solder bump locations. Lead and tin are co-plated onto the substrate through the  $20\text{-}\mu\text{m}$ -diam openings in the photoresist to form mushroom-shaped structures. The resist is stripped and then the copper and titanium are etched chemically using the solder as a mask. The solder is alloyed in a rapid thermal annealer at  $300^\circ\text{C}$  in a reducing ambient. Surface tension causes the solder to form the characteristic ball shape seen in Figure 4-3.

A chip and matching MCM substrate have been designed and fabricated to test this interconnect technique. The chip includes approximately 800 connections arranged around the perimeter on a  $50\text{-}\mu\text{m}$  pitch. A commercial aligner/bonder is used to attach the chips to the MCM substrate. This apparatus uses a combination of heat and pressure to bond the chips. We have achieved  $\pm 5\text{-}\mu\text{m}$  alignment accuracy and good contact resistance using this system. In an initial experiment using ten chips, none achieved 100% yield, but chains of approximately 100 good contacts were demonstrated. After electrical testing, some of the chips were removed from the MCM substrate and studied to determine causes for the failed connections. The electrical data and physical inspection of the solder bumps indicated that the mechanical contact was nonuniform across the chip, probably a result of a misalignment of the aligner/bonder. In future experiments the alignment tolerance will be improved by increasing the height of the solder bumps, and this should improve the yield.

S. Doran	D. Astolfi
A. Forte	T. M. Lyszczarz

## 4.2 SINGLE-LAYER RESISTS WITH ENHANCED ETCH RESISTANCE FOR 193-nm LITHOGRAPHY

A first-generation 193-nm photoresist [3] has been developed based on terpolymers of methyl methacrylate (MMA), *t*-butyl methacrylate (tBMA), and methacrylic acid (MAA). Single-layer (193 nm) resists based on these materials show photospeeds in the range 10 mJ/cm<sup>2</sup>, aqueous development in dilute tetramethyl ammonium hydroxide (TMAH), excellent contrast and imaging quality, and robust environmental stability. Unfortunately, the plasma etch resistance of methacrylate polymers is notoriously low. Our first-generation resist is no exception, with etch rates 2 to 2.5 times faster than novolac in aggressive (e.g., chlorine, hydrogen bromide) plasma environments. Workers at Fujitsu several years ago demonstrated substantial increases in etch resistance of methacrylate polymers through the introduction of aliphatic, cyclic (alicyclic) structures [4]. We have investigated the impact of alicyclic functionality on the etch properties, aqueous solubility, and glass transition temperature  $T_g$  of methacrylate copolymers.

One type of alicyclic functionality, which combines increased etch resistance with acid-catalyzed deprotection chemistry, is a methacrylate ester of isobornyl alcohol [5]. Since this "active" ester is thought to rearrange in the presence of photogenerated triflic acid to generate camphene after cleavage, it was considered to be a good starting point for an etch-resistant 193-nm resist.

To measure the response of isobornyl methacrylate (IBMA) incorporation on the etch rate of the methacrylate polymers, a series of IBMA-MMA copolymers were synthesized and characterized. Table 4-1 lists the charged monomer concentrations (in moles), the compositions found ( $C^{13}$  NMR), molecular weights, and  $T_g$  values. Note that the monomer feed and the polymer composition are quite similar, a sign that monomer reactivity in methacrylates is not a strong function of steric bulk. Note also that the free-radical solution polymerization offers good molecular weight control for methacrylate (co)polymer synthesis. The most striking feature of the polymer properties is the strong increase in  $T_g$  as a function of IBMA concentration [6]. The IBMA homopolymer has a  $T_g$  above 200°C. Polymers with appreciable levels of IBMA have a  $T_g$  above 150°C. The  $T_g$  of the resist has strong implications for its performance features, such as image thermal stability, mechanical properties, ability to anneal after spin coating, and impact on environmental stability [7].

Figure 4-4 shows the HBr plasma etch rate vs composition for the IBMA-MMA copolymer series. Under these aggressive etching conditions, the etch rate of PMMA is triple that of novolac. The IBMA homopolymer etches at a rate around 50% faster than novolac resin. This is a significant improvement, however, over the etch stability of conventional acrylic materials. A feature of considerable importance to resist designers is that the etch rate of the IBMA copolymers shows no deterioration until > 50 mol% of MMA is present in the copolymer. This finding offers appreciable latitude in the design of etch-resistant 193-nm resists, in that monomers that contribute to other resist properties (e.g., contrast, dissolution, thermal properties) can be incorporated in significant concentration.

IBMA homopolymer and IBMA-MMA copolymers are extremely hydrophobic, with good solubility in hexane and insolubility in polar solvents. As such, no aqueous development occurs even at high exposure doses (> 50 mJ/cm<sup>2</sup>). To achieve clean aqueous development in the methacrylate polymers, carboxylic acid functionality is typically supplied by MAA. A compositional window commonly exists for MAA content, below which the polymer is too hydrophobic, resulting in undeveloped residue and/or strong surface inhibition followed by rapid development which produces undercutting. The upper limit in MAA concentration manifests itself as an extremely fast unexposed thinning rate that is difficult to inhibit.

**TABLE 4-1**  
**Characteristics of MMA/IBMA Copolymers**

Monomer Feed (MMA/IBMA)	Polymer Composition	$M_n^*$	$M_w/M_n^*$	$T_g(^{\circ}\text{C})$
(100/0)	PMMA	21 000	1.8	115
(87/13)	(88.5/11.5)	24 000	1.7	137
(69/31)	72/28	24 000	1.7	148
(42.5/57.5)	46/54	27 000	1.7	170
(0/100)	PIBMA	18 200	1.9	203

*\* $M_n$  and  $M_w$  are number-average and weight-average molecular weight, respectively.*

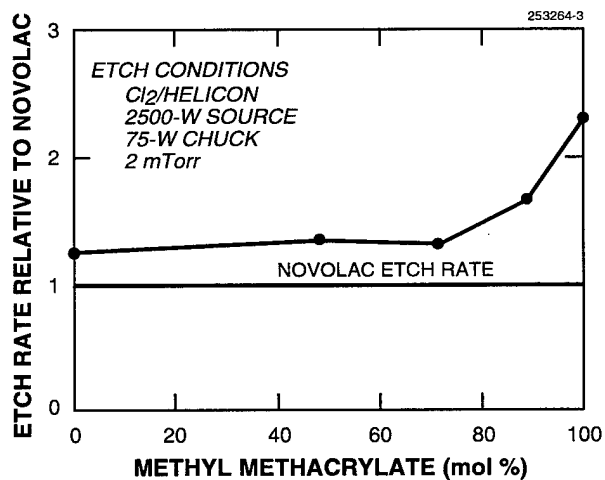


Figure 4-4. Etch rate of methacrylate copolymers as function of alicyclic content.

The hydrophobic/hydrophilic balance of the IBMA-based resist was modified through incorporation of MAA, a strategy employed with good results in the tBMA (first-generation) resist. The incorporation of MAA into the (high- $T_g$ ) IBMA polymer further increases the  $T_g$ . For example, IBMA-MAA (90/10) copolymer has a  $T_g$  of 217°C, while the more hydrophilic 75/25 (IBMA-MAA) copolymer has a  $T_g$  above decomposition (above 225°C). The extreme rigidity of these films is problematic. Any liquid, such as developer or water, contacting a coated wafer produces severe stress cracking of the film. The inability to anneal these films at or near  $T_g$  prohibits a simple processing technique to prevent cracking arising from locked-in stresses of these rigid materials. Acrylate polymers are known to possess a lower  $T_g$  than the corresponding methacrylate polymer. For example, the  $T_g$  of PMMA is 115–120°C, which is over 100°C higher than poly(methyl acrylate). Acrylate monomers were used to lower the  $T_g$  of the isoborneol resist system. The thermal properties of the methacrylate and acrylate isobornyl ester polymers (IBMA and IBA) vary markedly, and profoundly impact the imaging properties. The acrylate homopolymer IBA and copolymers with acrylic acid (IBA-AA), which have more attractive aqueous base development properties, have a  $T_g$  below 100°C. The low  $T_g$  in this polymer is coupled with the requirement of post-exposure baking at temperatures above 120°C, in order for the rearrangement to occur as discussed above. This implies long-range acid diffusion on the scale of millimeters when these exposed films are baked above the  $T_g$  to drive the deprotection chemistry. Physical mixtures of IBMA and IBA show characteristics associated with phase separation, even though structurally similar. The only method successfully employed to both increase hydrophilicity and bring the  $T_g$  into an acceptable range, which we define as 120–180°C, is the copolymer of IBMA-AA. For example, the 80/20 IBMA-AA copolymer has a  $T_g$  of 170°C and dissolves upon exposure and post-exposure baking in 0.26N TMAH.

Even though optimized IBMA-AA copolymers were prepared with acceptable  $T_g$  and aqueous developable characteristics, resolution better than 1  $\mu\text{m}$  was never achieved. We believe this was a result of the back reaction between the involatile leaving group (camphene) and the MAA to reform an isobornyl ester, thereby limiting the dissolution rate contrast. Incorporation of tBMA into the copolymer mix improves things somewhat, but further addition of monomeric dissolution inhibitors seems to be most critical. These three-component resist formulations benefit by addition of the monomeric inhibitors in three ways. First, the inhibitors vastly improve the dissolution rate contrast (nearly tenfold); second, they plasticize the high- $T_g$  resins, thereby reducing their  $T_g$  into the 140–160°C range; and third, they further improve the etch resistance by virtue of their alicyclic chemical structure. A preliminary result using this three-component approach was obtained by adding 25-wt% acetyl *t*-butyl lithocholate as the inhibitor to a tetrapolymer of IBMA, MMA, tBMA, and MAA. Resolution of 0.4  $\mu\text{m}$  was obtained, and the etch rate was reduced to only 20% of that of novolac.

R. D. Allen*	D. C. Hofer*
G. M. Wallraff*	R. R. Kunz
R. A. DiPietro*	

---

\*Author not at Lincoln Laboratory.

## REFERENCES

1. S. T. Riches, *Hybrid Circuits* **23**, 14 (1990).
2. Solid State Research Report, Lincoln Laboratory, MIT, 1991:4, p. 47.
3. Solid State Research Report, Lincoln Laboratory, MIT, 1993:2, p. 13.
4. Y. Kaimoto, K. Nozaki, S. Takechi, and N. Abe, *Proc. SPIE* **1672**, 66 (1992).
5. G. M. Wallraff, R. D. Allen, W. D. Hinsberg, C. F. Larson, R. D. Johnson, R. A. DiPietro, G. Breyta, and N. Hacker, *J. Vac. Sci. Technol. B* **11**, 2783 (1993).
6. A. Matsumoto, K. Mizuta, and T. Otsu, *J. Polym. Sci. Polym. Chem. Ed.* **31**, 2531 (1993).
7. H. Ito, W. P. England, R. Sooriyakumaran, N. J. Clecak, G. Breyta, W. D. Hinsberg, H. Lee, and D. Y. Yoon, *J. Photopolym. Sci. Technol.* **6**, 547 (1993).

## 5. HIGH SPEED ELECTRONICS

### 5.1 STAGGERED-BARRIER HETEROSTRUCTURE INSULATED-GATE FIELD-EFFECT TRANSISTOR ON InP

InP-based high-electron-mobility transistors (HEMTs) [1,2], heterostructure field-effect transistors (HFETs) [3,4], and heterostructure insulated-gate field-effect transistors (HIGFETs) [5,6] have become important recently, because of the growing interest in low-noise and low-power microwave and millimeter-wave integrated circuits. In these circuits, InP-based transistors are superior to the more conventional GaAs-based devices, largely because they contain channel materials, such as lattice-matched  $\text{In}_{0.53}\text{Ga}_{0.47}\text{As}$ , having significantly higher low-field electron mobility than GaAs. In addition, their channel and barrier materials, the common barrier being lattice-matched  $\text{In}_{0.52}\text{Al}_{0.48}\text{As}$ , provide much lower source and drain ohmic-contact resistance than  $n$ -type GaAs or AlGaAs. These features generally lead to transistors having a higher ratio of specific transconductance to gate capacitance, a higher unity-current-gain cutoff frequency, a lower small-signal noise figure, and a lower drain-source knee voltage separating the linear and active regions of operation.

One disadvantage of InP-based transistors compared to GaAs devices is their lower electrical strength, particularly the lower forward-bias gate turn-on voltage and the high gate leakage current. To alleviate these problems, we have developed a new HIGFET with an insulator containing alternating thin layers of AlAs and  $\text{In}_{0.52}\text{Al}_{0.48}\text{As}$  just above the  $\text{In}_{0.53}\text{Ga}_{0.47}\text{As}$  channel. Hence, we call the device a staggered-barrier heterostructure insulated-gate field-effect transistor (SB-HIGFET). This report deals only with a two-barrier version, but the design principles should apply to structures with more barriers.

The device in this work was grown by gas-source molecular-beam epitaxy on a semi-insulating (100)-oriented InP substrate at a temperature of  $500^\circ\text{C}$ . It consisted of the following epitaxial layers grown sequentially on the substrate: a 500-nm-thick undoped  $\text{In}_{0.52}\text{Al}_{0.48}\text{As}$  buffer layer, a 200-nm-thick undoped  $\text{In}_{0.53}\text{Ga}_{0.47}\text{As}$  channel layer, and a 30-nm-thick undoped insulator layer containing, just above the channel, two 2.0-nm-thick barriers of undoped AlAs separated by 2.0 nm of undoped  $\text{In}_{0.52}\text{Al}_{0.48}\text{As}$ . Between the AlAs barriers and the top of the structure was 24 nm of undoped  $\text{In}_{0.52}\text{Al}_{0.48}\text{As}$ . In addition to this structure, a control sample was grown that was identical to the SB-HIGFET structure, except that the AlAs barriers were replaced by undoped  $\text{In}_{0.52}\text{Al}_{0.48}\text{As}$  to maintain a total insulator thickness of 30 nm. After growth, FET structures were fabricated by standard microfabrication techniques. The resulting devices had metal gates  $1.5\text{ }\mu\text{m}$  long by  $100\text{ }\mu\text{m}$  wide and nominal gate-source and gate-drain separations of  $2.5\text{ }\mu\text{m}$ .

The dc characteristics of the two devices were measured at room temperature with a semiconductor parameter analyzer. Figures 5-1(a) and 5-1(b) show the common-source current-voltage characteristics of the control sample and the SB-HIGFET. Both devices are normally off and begin to conduct drain current with a small positive gate bias. The drain current of the control sample was 20 mA at a maximum gate voltage  $V_g = +2.5\text{ V}$ , which is typical for this type of HIGFET [5]. In contrast, the SB-HIGFET supports a drain current of  $\sim 60\text{ mA}$  at a maximum  $V_g$  of  $+3.5\text{ V}$ . Separate measurements of drain current on a finer scale yielded a gate threshold voltage of 0.0 and  $+0.2\text{ V}$  for the control device and SB-HIGFET, respectively. At a drain-source voltage  $V_{ds}$  of 2.0 V, the specific transconductance  $g_m$  of the control sample reached a peak value of 170 mS/mm at  $V_g = +0.5\text{ V}$  and dropped off rapidly at higher voltages, approaching zero just above  $V_g = +2.0\text{ V}$ . The drain current of the SB-HIGFET sample rose much more rapidly above threshold, showing a peak  $g_m$  of 290 mS/mm at  $V_g = +0.9\text{ V}$ . In addition, the  $g_m$  remained above 120 mS/mm for  $V_g$  up to  $+2.5\text{ V}$ . This is attributed to the superior electrical properties of the SB-HIGFET insulating layer.



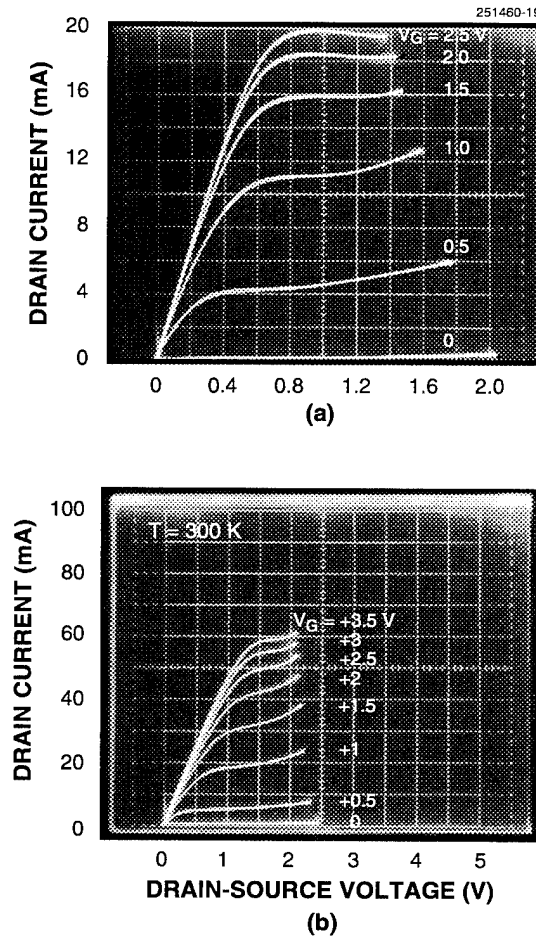


Figure 5-1. Room-temperature common-source current-voltage characteristics of (a) conventional  $\text{In}_{0.53}\text{Ga}_{0.47}\text{As}/\text{In}_{0.52}\text{Al}_{0.48}\text{As}$  heterostructure insulated-gate field-effect transistor (HIGFET) on InP substrate and (b) staggered-barrier (SB) HIGFET containing two 2.0-nm-thick AlAs barriers just above  $\text{In}_{0.53}\text{Ga}_{0.47}\text{As}$  channel.

To quantify the electrical strength of the gate, the forward-bias current was measured as a function of gate voltage with the source and drain contacts grounded. This condition is more strenuous on the gate insulator than the normal operating conditions (i.e., with the drain contact positively biased) because all regions of the channel under the gate, including the drain end, are at a much lower electrostatic potential than the gate contact. The results plotted in Figure 5-2 show that the gate current in the control device rises very rapidly, approaching 1.0 mA at  $V_g \approx +1.9$  V. Beyond this gate voltage the device began to break down. The SB-HIGFET draws much less gate current than the control sample, with  $\sim 50$  times lower current between  $V_g = +0.6$  and 1.2 V and roughly 10 times lower current at higher  $V_g$ . Figure 5-2 is also the basis for comparison with the results of normally-off InGaAs HIGFETs obtained by other groups.

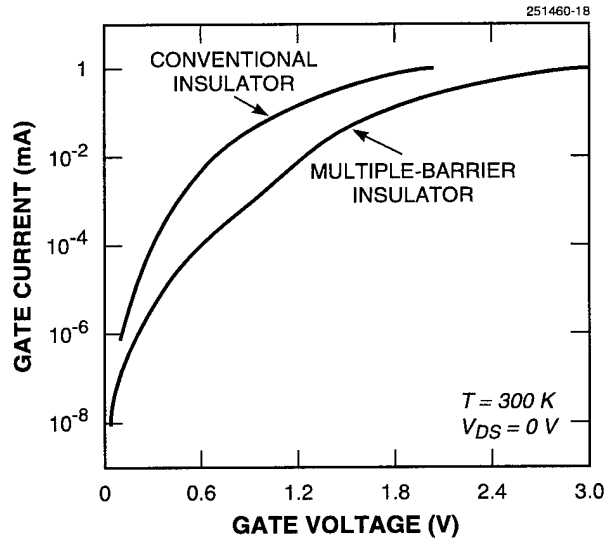


Figure 5-2. Room-temperature gate current vs gate voltage measured with drain and source contacts grounded for conventional  $\text{In}_{0.53}\text{Ga}_{0.47}\text{As}/\text{In}_{0.52}\text{Al}_{0.48}\text{As}$  HIGFET on InP substrate and SB-HIGFET containing two 2.0-nm-thick AlAs barriers just above  $\text{In}_{0.53}\text{Ga}_{0.47}\text{As}$  channel.

Using a heterostructure very similar to our control sample, Kamada et al. [5] obtained a gate leakage current of  $\sim 49 \text{ A cm}^{-2}$  at a gate voltage of +0.75 V and with the source and drain contacts grounded. Using a structure with a 40-nm-thick insulator, Feuer et al. [6] obtained a gate leakage of  $4.0 \text{ A cm}^{-2}$  under the same bias conditions. These results straddle our value of  $10 \text{ A cm}^{-2}$  at  $V_g = +0.75 \text{ V}$  for the control sample.

The superior overall characteristics of the SB-HIGFET are attributed to improved charge confinement in the channel. In principle, the  $\text{In}_{0.52}\text{Al}_{0.48}\text{As}/\text{AlAs}$  heterostructure reduces the gate current at large forward bias by suppressing the thermionic emission of electrons in the channel over the  $\Gamma$ -point barrier of the insulator. This follows from the fact that AlAs provides a  $\Gamma$ -point conduction band offset of  $\sim 1.56 \text{ eV}$  (assuming lattice-matched AlAs) relative to  $\text{In}_{0.53}\text{Ga}_{0.47}\text{As}$ , compared to an offset of just  $0.39 \text{ eV}$  for  $\text{In}_{0.52}\text{Al}_{0.48}\text{As}$  relative to  $\text{In}_{0.53}\text{Ga}_{0.48}\text{As}$ . Furthermore, the 3.5% lower lattice constant of AlAs forces it into lateral tension, which makes the  $\Gamma$ -point offset even higher.

E. R. Brown	C. L. Chen
L. J. Mahoney	P. A. Maki
K. B. Nichols	

## REFERENCES

1. L. D. Nguyen, A. S. Brown, M. A. Thompson, and L. M. Jelloian, *IEEE Trans. Electron Devices* **39**, 2007 (1992).
2. J. B. Shealy, M. M. Hashemi, K. Kiziloglu, S. P. DenBaars, U. K. Mishra, T. K Liu, J. J. Brown, and M. Lui, *IEEE Electron Device Lett.* **14**, 545 (1993).
3. S. R. Bahl, B. R. Bennett, and J. A. del Alamo, *IEEE Electron Device Lett.* **14**, 22 (1993).
4. Y-J. Chan and D. Pavlidis, *IEEE Trans. Electron Devices* **39**, 466 (1992).
5. M. Kamada, H. Ishikawa, and M. Feng, *IEEE Trans. Electron Devices* **40**, 1358 (1993).
6. M. D. Feuer, D. M. Tennant, J. M. Kuo, S. C. Shunk, B. Tell, and T. Y. Chang, *IEEE Electron Device Lett.* **10**, 70 (1989).

## 6. MICROELECTRONICS

### 6.1 IMPROVED SOFT X-RAY QUANTUM EFFICIENCY FOR BACK-ILLUMINATED IMAGER

Several difficulties are posed by imaging a wide spectrum of x-rays in missions such as the Advanced X-ray Astrophysics Facility. Charge-coupled device (CCD) imagers may be used in the soft x-ray region of the spectrum, but can suffer because of photon absorption in the polysilicon gate structure. On the other hand, the absorption length of hard x-rays is on the order of  $40\text{ }\mu\text{m}$  and so requires a depleted Si region of this thickness. One possible solution to this dilemma is to employ a back-illuminated imager that is  $\sim 40\text{ }\mu\text{m}$  thick. A back-illuminated CCD imager should have a superior response to soft x-rays if an electric field drives minority carriers toward the buried channel of the CCD and if surface states on the back surface of the CCD are suppressed. A technique that uses this strategy to improve the response of back-illuminated CCDs to ultraviolet light [1] was implemented on high-resistivity wafers in such a way as to prevent the generation of plastic slip [2]. Briefly, the process consists of thinning a CCD wafer, implanting B into the back surface of the wafer, and passivating this surface. At all steps in the process, care is exercised to avoid generating stresses in the wafer due to thermal gradients or overlying layers.

Since the C K $\alpha$  x-ray at 277 eV has an absorption depth of  $\sim 100\text{ nm}$ , imaging its photons is a sensitive test of the CCD's ability to collect soft x-rays and to determine their energy. This energy is quantified by counting the number of electrons in a pixel and assuming that one electron is generated for every 3.65 eV in the absorbed photon. Some photoelectrons may, however, diffuse laterally into another pixel before they are collected in the buried channel of the CCD, leading to less electrons in a given pixel than the theoretical value. The results of exposing a back-illuminated CCD to a C K $\alpha$  source are shown in Figure 6-1, where the abscissa is the energy corresponding to the number of electrons and the ordinate is the count of pixels containing this

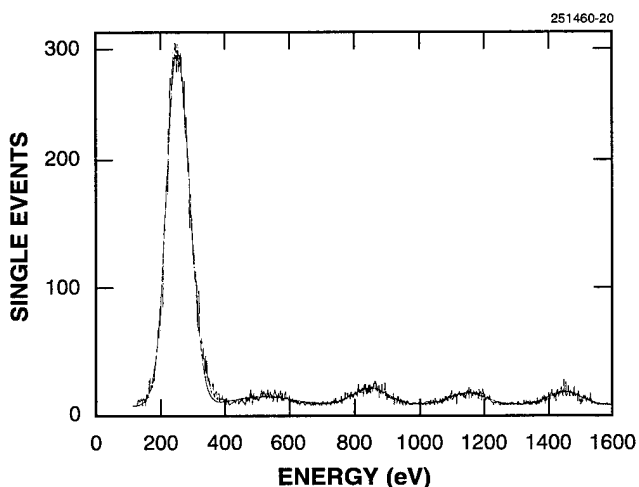


Figure 6-1. Frequency of single events vs energy for back-illuminated imager exposed to C K $\alpha$  x-rays.

number of electrons. The full width at half-maximum (FWHM) for the C K $\alpha$  peak is 83 eV for this sample, which is  $\sim 45\text{ }\mu\text{m}$  thick. For a  $20\text{-}\mu\text{m}$ -thick sample the FWHM is 62 eV, while it is 42 eV for a front-illuminated CCD. This decrease in FWHM for decreasing thickness is expected, as the electrons have a reduced opportunity to diffuse laterally before being collected in the buried channel. The FWHM of the front-illuminated device may be considered the minimum achievable in practice, but a width of 83 eV is adequate for x-ray spectroscopy and will allow the elemental source of the x-ray to be identified.

The absolute quantum efficiency was about 70% for both back-illuminated devices and 1% for the front-illuminated device. A thinned wafer prepared without the passivation layer on the back surface had a quantum efficiency of only 30% and much greater lateral diffusion of the photoelectrons. Similar results were obtained using the O K $\alpha$  peak, which penetrates  $\sim 500\text{ nm}$  into Si, indicating that use of the full process for back-illuminated chips gives a substantial advantage in imaging light element x-ray sources.

The large number of single events measured indicate the  $45\text{-}\mu\text{m}$ -thick devices are fully depleted through their thickness. Considering this, the thicker back-illuminated chip offers an advantage over the thinner in presenting a greater thickness to absorb the x-rays from more energetic sources, such as Fe and heavier elements.

J. A. Gregory	A. H. Loomis
B. E. Burke	G. Prigozhian*

## REFERENCES

1. J. A. Gregory, B. E. Burke, A. H. Loomis, and H. R. Clark, Solid State Research Report, Lincoln Laboratory, MIT, 1993:1, p. 53.
2. J. A. Gregory and R. W. Mountain, Solid State Research Report, Lincoln Laboratory, MIT, 1994:2, p. 49.

---

\*Author not at Lincoln Laboratory.

## 7. ANALOG DEVICE TECHNOLOGY

### 7.1 ANALYSIS OF THE QUANTUM FLUX PARAMETRON FOR SENSING SMALL CURRENTS AT HIGH BANDWIDTHS

The quantum flux parametron (QFP), a Josephson-junction superconductive electronic circuit, was invented by Eiichi Goto [1]. As fast, highly sensitive comparators, QFPs have exhibited sensitivities of  $1\ \mu\text{A}$  with switching times approaching 1 ps [2]. A QFP-based race arbiter, a circuit that decides which of two pulses arrived first, demonstrated an rms discrimination-time jitter of  $\pm 0.3$  ps [3]. QFPs can also be used as general digital elements [4]. A QFP shift register, for example, has been proposed to operate at 36 GHz [5].

The schematic diagram of a QFP comparator is shown in Figure 7-1. It is formed by shunting a two-junction superconducting quantum interference device (SQUID) with an inductor  $L_{\text{out}}$ . Two input currents are applied to the QFP, a signal input and an exciter input. The QFP is operated by first applying a positive or negative signal input, which may be very small, and then ramping up the exciter input. The following is a simplified view of how the QFP works. The exciter acts as a control current to the SQUID, reducing its critical current. When the critical current becomes smaller than the magnitude of the SQUID bias current that is injected by the signal, the QFP enters an unstable state. It then undergoes a transition that changes the magnetic flux in the circuit by a single quantum  $\Phi_0$ , delivering a large current  $i_{\text{out}}$  to the output inductor  $L_{\text{out}}$ .

For a positive signal current a magnetic flux quantum of clockwise-circulating current enters the left loop of the QFP comprising circuit elements  $J_1$ ,  $L_1$ , and  $L_{\text{out}}$ , and for a negative signal a clockwise flux quantum enters the right loop of the QFP comprising elements  $J_2$ ,  $L_2$ , and  $L_{\text{out}}$ . As a result the output current flows in the same direction as the signal current, but the magnitude is much larger.

Operation of the QFP can be understood qualitatively in another way from Figure 7-2, where the potential energy of the QFP is plotted as a function of the magnetic flux  $\Phi$  in the output inductor. In Figure 7-2(a), neither the signal nor the exciter has been applied. The equilibrium state, indicated by the dot, is in the center of the potential well, corresponding to zero flux in the output inductor. When a small signal is applied, the potential energy function shifts slightly to the right, as shown in Figure 7-2(b). The effect of the exciter current is to flatten the potential well, as seen in Figure 7-2(c), and then to push up a ridge in the center. Ultimately, two energy minima are formed, as shown in Figure 7-2(d), each of which is a system equilibrium state. The sign of the initial signal current determines which of these two equilibria the QFP will settle into. With perfectly matched components and no thermal noise, an infinitesimally small signal current will result in a large final output current. Thus, the gain of the circuit is very high. For a typical QFP operating at a temperature of 4.2 K, a signal current with a magnitude as small as  $1\ \mu\text{A}$  is sufficient to ensure deterministic switching when the exciter current is applied slowly compared to the intrinsic switching time of the QFP [2].

We are interested in using QFPs for two superconductive electronics subsystems. The programmable filter for a 2-gigachip-per-second spread-spectrum modem requires a current discriminator in the analog output summing bus. The QFP may be the only circuit with high enough sensitivity for this task. Another subsystem, the crossbar switch, employs an array of QFPs that detect and amplify channels of  $40\text{-}\mu\text{A}$  digital data pulses, which arrive at 2 Gbit/s. We need to optimize the QFP design so that an entire array of them will function despite typical process variations in component values.

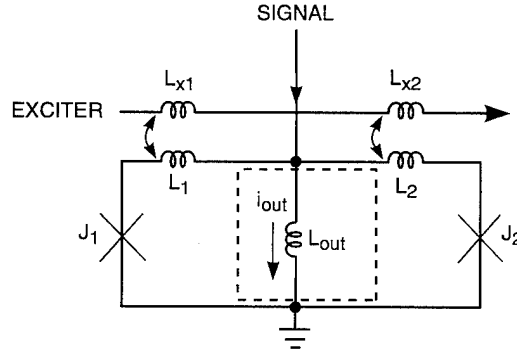


Figure 7-1. Schematic diagram of quantum flux parametron (QFP) used as current comparator. The dashed line surrounds the output inductor to emphasize that it is a shunt across the SQUID loop comprising the elements  $J_1$ ,  $L_1$ ,  $L_2$ ,  $J_2$ .

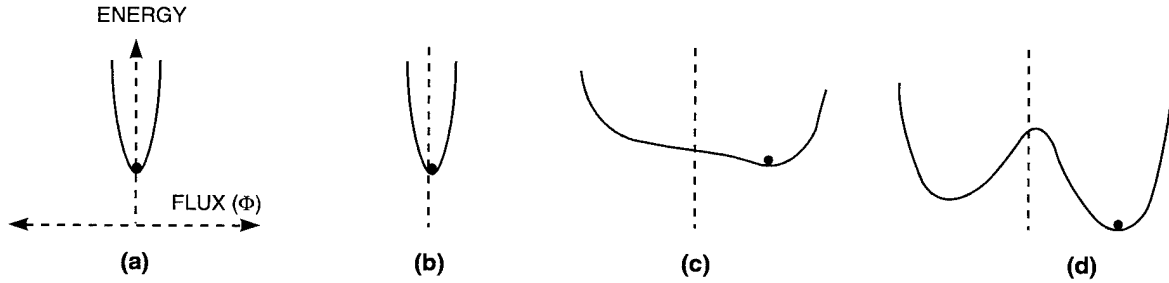


Figure 7-2. Potential energy plots of QFP for different input/exciter conditions. The abscissa is the magnetic flux ( $\Phi$ ) in the output inductor  $L_{out}$ . In (a) neither the input nor the exciter current has been applied. Then a small negative input current is applied in (b). In (c) we have begun to ramp up the exciter, and in (d) the exciter is at its final value.

To aid in the optimization of QFP designs, we have implemented an algorithm to compute the final, steady-state output current  $i_{out}$  as a function of the signal and exciter currents. We used the slightly modified schematic shown in Figure 7-3, in which the signal current is transformer-coupled into the QFP, because this is how our actual circuits are implemented. Figure 7-3 defines the following parameters used in our analyses: the critical currents of the junctions,  $I_{c1}$  and  $I_{c2}$ ; the two SQUID inductances,  $L_1$  and  $L_2$ ; the output inductance,  $L_{out}$ ; the phases across the junctions,  $\phi_1$  and  $\phi_2$ ; the phase across the output inductor,  $\phi$ ; the currents through the junctions,  $i_1$  and  $i_2$ ; and the current in the output inductor,  $i_{out}$ .

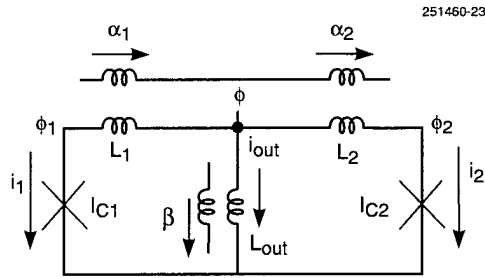


Figure 7-3. Schematic diagram of QFP showing terminology used to compute the static solutions. The exciter current couples  $\alpha_1$  radians of phase into the inductor  $L_1$  and  $\alpha_2$  radians of phase into the inductor  $L_2$ . The input couples  $\beta$  radians of phase into the inductor  $L_{out}$ .

To simplify our analysis we treat the signal and exciter inputs as phase sources that contribute quantum-mechanical phase drops to their respective inductors, rather than as current sources that deliver currents into the QFP. We can do this because of the following two relationships: a current  $i$  flowing through an inductance  $L$  generates a magnetic flux  $Li$  and a phase drop  $Li(2\pi/\Phi_0)$ , and a current  $i$  flowing in one winding of a transformer with mutual inductance  $M$  couples into the other winding a magnetic flux  $Mi$  and a phase drop  $Mi(2\pi/\Phi_0)$ . The exciter current induces two separate but proportional phase drops,  $\alpha_1$  and  $\alpha_2$ , into the two arms of the QFP, while the signal current induces a phase drop  $\beta$  into the output inductor. Our goal is to solve for the output current  $i_{out}$  as a function of the signal phase  $\beta$  and the exciter phases  $\alpha_1$  and  $\alpha_2$ .

Rather than trying to solve directly the equations that describe the circuit, we adopted a straightforward approach based on self-consistency. For a given set of component values ( $L_{out}$ ,  $L_1$ ,  $L_2$ ,  $I_{c1}$ ,  $I_{c2}$ ) and excitation/signal values ( $\alpha_1$ ,  $\alpha_2$ ,  $\beta$ ), our C code performs the following computation. First, a value of  $\phi_1$  is chosen. From the Josephson junction current equation  $i_1 = I_{c1} \sin \phi_1$  we can compute the current in the left junction. Since the same current flows through the inductor  $L_1$ , we can calculate the phase drop across it, taking into account the contribution  $\alpha_1$  of the exciter. Now we know the phase  $\phi$  at the top of the output inductor, and taking into account the phase contribution  $\beta$ , we can calculate the current  $i_{out}$  flowing in the inductor  $L_{out}$ . Given the currents  $i_1$  and  $i_{out}$ , we can calculate the current  $i_2$  that flows through the inductor  $L_2$ , and taking into account  $\alpha_2$ , can determine the phase  $\phi_2$ . Now comes the critical test. Using the value of  $\phi_2$ , we can calculate the current  $i_2$  from the Josephson current equation  $i_2 = I_{c2} \sin \phi_2$ . If this value of  $i_2$  agrees—within some tolerance—with the value we determined earlier, then we mark the value of  $i_{out}$  as a solution.

The above procedure is followed for a range of initial choices for  $\phi_1$ , stepping  $\phi_1$  in small increments. We can set bounds on the range of  $\phi_1$  values that need to be considered. An upper bound can be found as follows. Because the maximum currents that can flow in the junctions are  $I_{c1}$  and  $I_{c2}$ , the maximum current that can possibly flow in  $L_{out}$  is  $I_{c1} + I_{c2}$ . This implies a maximum phase  $\phi$  at the top of  $L_{out}$  of

$$\beta + L_{out}(I_{c1} + I_{c2})(2\pi/\Phi_0) . \quad (7.1)$$



The maximum current that can flow in  $L_1$  is  $I_{c1}$ , and thus the maximum phase drop across  $L_1$  is

$$\alpha_1 + L_1 I_{c1} (2\pi/\Phi_0) . \quad (7.2)$$

By summing the maximum phase drop across  $L_1$  to the maximum value of  $\phi$ , we can place an upper bound on  $\phi_1$  of

$$\alpha_1 + \beta + [L_1 I_{c1} + L_{\text{out}}(I_{c1} + I_{c2})](2\pi/\Phi_0) . \quad (7.3)$$

Similarly, we can supply a lower bound for  $\phi_1$  of

$$\alpha_1 + \beta + [L_1 I_{c1} + L_{\text{out}}(I_{c1} + I_{c2})](2\pi/\Phi_0) . \quad (7.4)$$

Within this range of  $\phi_1$  values we may, and often do, find more than one solution.

Figure 7-4(a) shows the results of an analysis, with  $I_{c1} = I_{c2} = 225 \mu\text{A}$ ,  $L_1 = L_2 = 0.9 \text{ pH}$ ,  $L_{\text{out}} = 4.1857 \text{ pH}$ , and  $\beta = 0.1 \text{ rad}$ . The horizontal axis spans the range  $\alpha_1 = \alpha_2 \equiv \alpha = \{-2\pi, 2\pi\}$ , and the vertical axis shows the corresponding solutions for the current output  $i_{\text{out}}$ . Note that multiple solutions exist around  $\alpha = \pi$ . Our algorithm cannot discern between stable and unstable equilibria, and thus Figure 7-4(a) shows both types of solutions. To eliminate the unstable equilibria, we have added a post-processor to our C code. For a given solution, we evaluate the Hessian [6] of the potential energy function [2] with respect to the sum and difference of the junctions' phases ( $\phi_1$  and  $\phi_2$ ) to determine whether or not the potential energy of the system is a minimum, a maximum, or a saddle point. Where the Hessian is positive definite, the solutions are stable minima, and these are shown in Figure 7-4(b).

Note in Figure 7-4(b) that when  $\alpha = \pi$ , only two stable solutions exist, one positive and one negative. If we apply the input signal  $\beta = 0.1$  first, followed by the exciter  $\alpha = \pi$ , then we end up in the equilibrium state with the positive output current. For a negative signal  $\beta = -0.1$  the plot is mirrored about the horizontal axis, and we end up in the negative output current state. The plot also shows that, as expected, the QFP is periodic in its response to the exciter phase with a period of  $2\pi \text{ rad}$ . This static simulation shows the entire set of possible states for the given value of  $\alpha$  but does not tell which state will actually be occupied. That information was determined by running a dynamic simulation of the QFP using JSIM [7]. To validate the correctness of our approach and its implementation in C code, we checked several of the static solutions against the results of full dynamic simulations. The agreement was essentially perfect. One advantage of our static analysis is that it computes the final state for each set of circuit parameters in a fraction of the time that a dynamic simulator would take. Thus, we can reduce hours of computation down to a few minutes. A second advantage is that it finds all possible solutions, not just the one that results from a particular set of initial conditions and input waveforms.

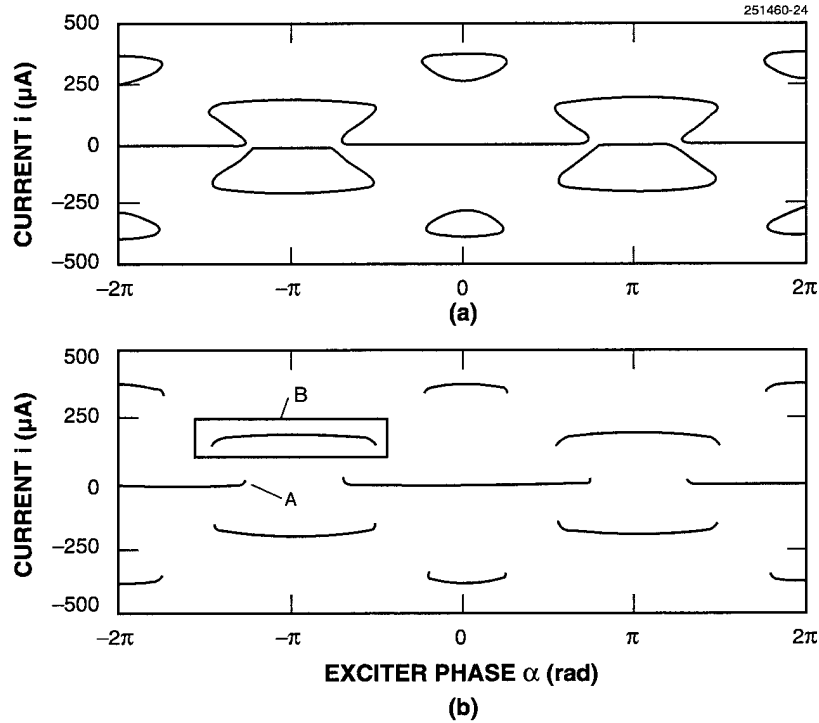


Figure 7-4. Plots of QFP solutions for circuit parameters:  $L_1 = L_2 = 0.9 \text{ pH}$ ,  $I_{c1} = I_{c2} = 225 \text{ }\mu\text{A}$ ,  $L_{out} = 4.1857 \text{ pH}$ ,  $\beta = 0.1 \text{ rad}$ ,  $\alpha = \{-2\pi, 2\pi\}$ . In (a) we show all solutions and in (b) we show only stable equilibria.

Plots like those in Figure 7-4(b) reveal behavioral details that would not be readily apparent from individual dynamic simulations. For example, we can determine the minimum amount of exciter phase needed to get the QFP to switch (point A) and can see how wide the range of exciter currents is and how little the variation in the output current is for the switched state (region B). Because our program generates such plots very quickly, we can study how the behavior of the QFP changes when parameters are varied, either by design or as a result of process variation. For example, we have determined the dc signal current offset required to rebalance the signal input of a QFP whose junction critical currents ( $I_{c1}$ ,  $I_{c2}$ ) or whose arm inductances ( $L_1$ ,  $L_2$ ) are unequal. In general, our analysis can be used to optimize the design and to determine the allowable process tolerances.

D. A. Feld  
J. P. Sage

## REFERENCES

1. W. Hioe and E. Goto (eds.), *Quantum Flux Parametron: A Single Quantum Flux Superconducting Logic Device* (World Scientific, Singapore, 1991).
2. H. L. Ko and G. S. Lee, *IEEE Trans. Appl. Superconduct.* **2**, 156 (1992).
3. G. S. Lee, R. C. Ruby, H. L. Ko, and A. T. Barfknecht, *Appl. Phys. Lett.* **59**, 2892 (1991).
4. M. Hosoya, W. Hioe, J. Casas, R. Kamikawai, Y. Harada, Y. Wada, H. Nakane, R. Suda, and E. Goto, *IEEE Trans. Appl. Superconduct.* **1**, 77 (1991).
5. M. Hosoya, W. Hioe, K. Takagi, and E. Goto, to be published in *IEEE Trans. Appl. Superconduct.* **5** (1995).
6. J. E. Marsden and A. J. Tromba, *Vector Calculus*, 2nd ed. (W.H. Freeman, San Francisco, 1981).
7. E. S. Fang and T. Van Duzer, *JSIM Preliminary Version User's Guide* (University of California, Berkeley, 1991).

